

2018-10-01

Size-resolved aerosol fluxes above a temperate broadleaf forest

A. Petroff, J.G. Murphy, S.C. Thomas, J.A. Geddes. 2018. "Size-resolved aerosol fluxes above a temperate broadleaf forest." *ATMOSPHERIC ENVIRONMENT*, Volume 190, pp. 359 - 375 (17). <https://doi.org/10.1016/j.atmosenv.2018.07.012>

<https://hdl.handle.net/2144/39495>

"Downloaded from OpenBU. Boston University's institutional repository."

Size-resolved aerosol fluxes above a temperate broadleaf forest

A. Petroff^{a,c}, J.G. Murphy^a, S.C. Thomas^b, J.A. Geddes^{a,d}

^a*University of Toronto, Department of Chemistry, 80 St George Street, Toronto, Ontario M5S 3H6, Canada*

^b*University of Toronto, Faculty of Forestry, 33 Willcocks Street, Toronto, Ontario M5S 3B3, Canada*

^c*Now at Centre Régional de la Propriété Forestière d'Occitanie, La Milliasolle, BP 89, 81003 Albi Cedex*

^d*Now at Boston University, Department of Earth and Environment, 685 Commonwealth Ave, Boston, MA, 02215*

Abstract

Aerosol fluxes were measured by eddy-correlation for 8 weeks of the summer and fall of 2011 above a temperate broadleaf forest in central Ontario, Canada. These size-resolved measurements apply to particles with optical diameters between 50 and 500 nm and are the first ones reported above a temperate deciduous forest. The particle spectrometer was located on top of the flux tower in order to reduce signal dampening in the tube and thus maximize measurement efficiency. The 8-week data set extends into autumn, capturing leaf senescence and loss, offering a rare opportunity to investigate the influence of leaf area index on particle transfer. A distinct pattern of emission and deposition that depends on the particle size is highlighted : while the smallest particles ($d_p < 100$ nm) are preferentially emitted (55 % of the time), the largest particles ($d_p > 100$ nm) are preferentially deposited (62 % of the time). For the size bins with detection efficiency above 50 % (68-292 nm), the median transfer velocity for each bin varies between +1.34 and -2.69 mm.s⁻¹ and is equal to -0.21 mm.s⁻¹ for the total particle count. The occurrence of the upward fluxes shows a marked diurnal pattern. Possible explanations for these upward fluxes are proposed. The

*Corresponding author

Email address: alexandre_petroff@yahoo.fr (A. Petroff)

measurements, and their comparison with an existing model, highlight some of the key drivers of the particle transfer onto a broadleaf forest: particle size, friction velocity, leaf area index and atmospheric stability.

Keywords: particle flux, fine particle, broadleaf forest, transfer velocity, eddy correlation, modelling, leaf senescence

Introduction

Airborne particles contribute to the radiation balance of the atmosphere and to the cycling of chemicals between the atmosphere and the terrestrial surface. In particular, the deposition of nitrogen, partly in the aerosol phase, has a fertilizing effect on plant growth in nitrogen-limited systems, but can also lead to the acidification of the soil and the eutrophication of bodies of water located downstream (Fowler et al., 2009, and references herein). An accurate evaluation of such impacts requires knowledge of the vertical transfer of particles between the atmosphere and the earth. However, the magnitude of this particle transfer and its drivers remain uncertain, despite some 30 years of modelling efforts (Davidson et al., 1982; Zhang et al., 2001; Petroff and Zhang, 2010) and improvements in particle measurements based on eddy-correlation techniques (Wesely et al., 1985; Lamaud et al., 1994; Gallagher et al., 1997; Buzorius et al., 2000; Held et al., 2007; Pryor et al., 2009; Mammarella et al., 2011; Farmer et al., 2011; Deventer et al., 2015).

The vast majority of existing particle flux campaigns by eddy-correlation over forests have been based on the determination of a total particle number flux, mostly with a Condensation Particle Counter (CPC) and the simultaneous measurement of the aerosol number size distribution through a particle sizer (Buzorius et al., 2000; Held et al., 2007; Mammarella et al., 2011). The influence of particle size on deposition can then only be inferred. Faster samplers have been developed in the last decade and measurements of direct size-resolved particle number flux are being gathered in temperate coniferous forests (Gallagher et al., 1997; Vong et al., 2010; Deventer et al., 2015) and only rarely in tem-

perate broadleaf forest (Pryor et al., 2009, on particles smaller than 100 nm) or
25 mixed forest (Gordon et al., 2011).

A parallel research path has been followed by the community of Aerosol Mass Spectrometry, which is studying the chemically-determined mass flux of the atmospheric aerosols (Thomas, 2007; Nemitz et al., 2008; Gordon et al., 2011; Farmer et al., 2011, 2015). Though not size-segregated, these results provide
30 extremely valuable information on the processes involved in the atmosphere-forest aerosol exchange and composition for particles between 50 and 1000 nm. The present study is part of a scientific project studying the cycles of carbon and nitrogen in a remote temperate hardwood-dominated forest in central Ontario, Canada. Although local sources of nitrogen are scarce, regional estimates
35 of nitrogen deposition are suspected to be among the highest in North America (Environment Canada, 2004), and observations suggest that dominant trees at this site and regionally have transitioned to phosphorus limitation (Gradowski and Thomas, 2006, 2008).

To our knowledge, this is the first size-resolved measurement campaign of accumulation mode particle fluxes over a temperate broadleaf forest. The goals
40 of this study are to help understand the dynamics of particle exchange between the atmosphere and the forest and its main drivers. The campaign extended into the fall in order to gain insights on the influence of leaf senescence and loss on particle flux, which to our knowledge has not been documented.

45 1. Site and methods

1.1. Description of the study site

The site is located in Haliburton Forest and Wildlife Reserve in central Ontario (45.2866°N, 78.5387°W). Land morphology is relatively homogeneous with an undulating topography on the granitic Canadian Shield. Assessment of
50 the turbulence homogeneity and full development was part of the flux quality control (see Section 1.6). The average annual precipitation for the area is 1050 mm and the mean annual temperature is 5°C (Environment Canada). A 32-

m tall instrument tower is located at ~ 500 m above sea level on a plateau area 300 m away from wetlands and 1 km away from a lake. A 100 m steep ridge is located to the north-northwest (Fig. 1). Prior measurements at the site have included eddy-correlation and chamber-based estimates of methane flux (Wang et al., 2013), nitrogen flux (Geddes and Murphy, 2014) and eddy-correlation measurements of carbon and water vapour (Geddes et al., 2014). Flux measurements were performed for about 8 weeks from August 16th, 2011 to October 10th, 2011. A diesel generator was used to power equipment during this intensive study and was located 70 m north of the tower. The northern wind sector ($\pm 45^\circ$) was thus excluded from the analysis.

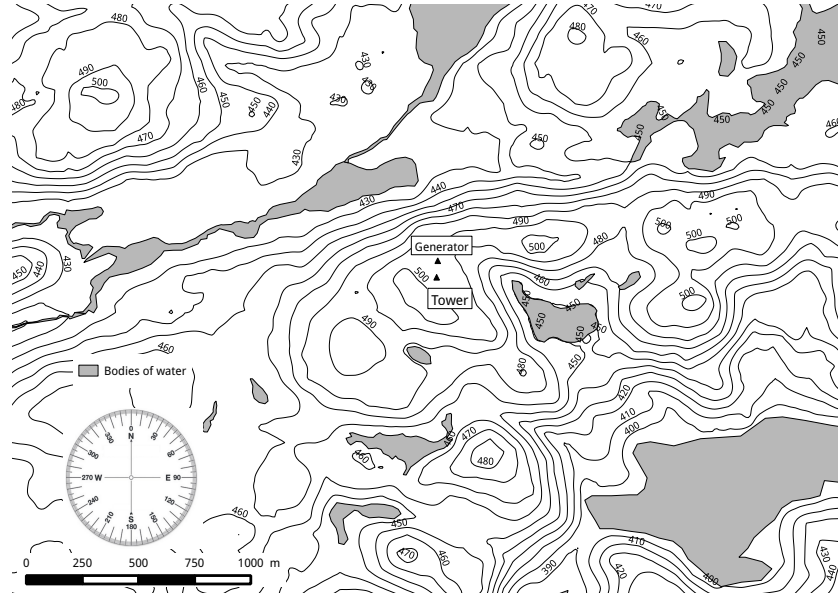


Figure 1: Location of the flux tower. The sonic orientation is 215° . Contours correspond to altitude above mean sea level.

The site vegetation consists of an uneven-aged managed forest dominated by Sugar maple (*Acer saccharum* Marsh) and American beech (*Fagus grandifolia* Ehrh.). The canopy height ranges from 20 to 25 m, with an average height of 22

m. The most recent harvest took place in 1996-1997, and the stand was affected by a large windstorm in 1995. Basal area (measured 2013) is $19.7 \text{ m}^2.\text{ha}^{-1}$ (with bootstrapped 95% confidence limits of $17.8\text{-}21.4 \text{ m}^2.\text{ha}^{-1}$). Leaf area index (LAI) measurements were made using litter traps positioned on a grid within 150 m of the flux tower, and seasonal changes in LAI were monitored at an approximate 2-week sampling interval using the TRAC instrument method (Chen and Cihlar, 1995). This plant canopy gap-size analyzer was walked under the canopy along transects to quantify the fraction of photosynthetically active radiation absorbed by plant canopies, the leaf area index and canopy architectural parameters. Peak 2011 LAI (two-sided) was 13, and TRAC measurements indicated a decline in LAI of 70% by the end of the measurement campaign. *Acer saccharum* and *Fagus grandifolia* made up $\sim 95\%$ of leaf area in the stand; other species present include *Betula alleghaniensis*, *Ostrya virginiana*, *Tsuga canadensis*, *Acer pensylvanica*, and *Picea spp* (Geddes et al., 2014). The displacement height d is estimated as 16.5 m (Raupach, 1994; Harman and Finnigan, 2007). The roughness length is evaluated using the formula emphasized by Lumley and Panofsky (1964) under near-neutral conditions:

$$z_0 = (z_R - d) \exp\left(\frac{-\overline{u_R}}{\sigma_u}\right), \quad (1)$$

where $\overline{u_R}$ is the mean horizontal wind at the reference height z_R . The roughness
65 length was estimated to be $z_0 = 1.5 \pm 0.7\text{m}$.

1.2. Instrumentation

Half-hourly fluxes of momentum, sensible heat and latent heat were measured using an open path system consisting of a CSAT3 sonic anemometer (Campbell Scientific, Canada), a LI-7500 infrared H_2O gas analyzer (LI-COR),
70 and an HMP45C temperature and humidity probe. Size-resolved particle number concentrations were measured using a Ultra High Sensitivity Aerosol Spectrometer (UHSAS, Droplet Measurement Technologies, USA, operating with a 1054 nm wavelength laser), counting particles with optical diameter between 55 and 1000 nanometers at 10 Hz. For this study, the 100 original size bins were

75 aggregated into the 14 following bins (in nm): 055-068, 068-083, 083-102, 102-125, 125-153, 153-188, 188-231, 231-292, 292-359, 359-440, 440-541, 541-664, 664-815 and 815-1000.

The aerosol sampler was located on the top of the tower, at 32 m, in an enclosure located 4 meters away from the sonic anemometer. The enclosure allowed
80 for air circulation around the instrument by use of 3 fans. Direct heating from the sun was limited by placing the enclosure under a rain shelter and covering it with aluminum foil. Condensation inside the enclosure was avoided by placing large desiccant packs (Desipack, Sud-Chemie, Germany) in the box and changing them as soon as they showed signs of saturation (usually every other
85 day). The stainless steel lines were also insulated from direct sun-light with foam rubber.

The aerosol inlet was located 1 m away from the sonic anemometer(longitudinal and vertical distances of 80 cm and 55cm). The thin-wall conic nozzle was inclined at 20° from the horizontal. The flow was set at 37 L.min⁻¹ through 3.56 m
90 of stainless steel (SS) line of 1.1 cm inside diameter (ID) (Fig. 2). The Reynolds number of the flow corresponded to a fully developed turbulence ($Re_D \sim 4800$). The flow was then split in two, 5 L.min⁻¹ going through 0.07 m of the same 1.1 cm ID SS to another instrument (APS, TSI, USA), whose measurements will not be exploited in the present paper. The second flow (32 L.min⁻¹) went
95 through another 0.16 m of the same 1.1 cm ID SS before a pipe reduction to a 0.35 cm ID SS line, with 0.37 m separating the reduction from the UHSAS inlet. The Reynolds number of the flow in this section also corresponded to fully developed turbulence ($Re_D \sim 12900$). The UHSAS inlet pulled at 75 cm³.min⁻¹ and the rest of the flow was by-passed to the pump by a "T-run" union. The
100 distance between the "T-run" and the entrance of the laser chamber was 2 cm. The sheath flow was set at 700 cm³.min⁻¹. We did not dry the flow prior to sampling. Two coalescing filters (SMC, USA) were mounted inside the UHSAS to dry the recirculating sheath flow. These filters were needed because the forest environment was very humid, potentially resulting in accumulation of water in
105 the sheath flow lines, which may degrade the mirrors' reflectance.

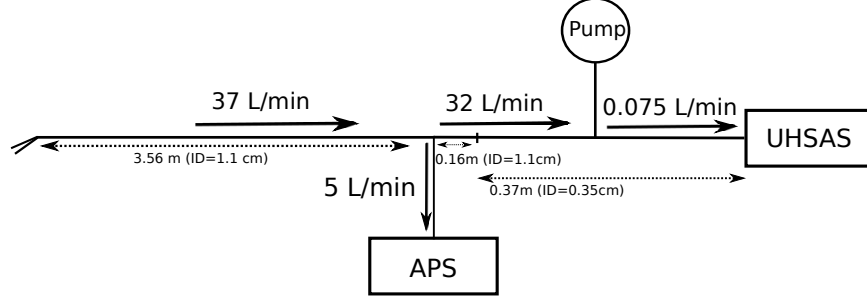


Figure 2: Diagram of the experimental set-up

The UHSAS had its own internal PC capable of logging data at 10 Hz. The sonic anemometer and gas-analyzer were connected to a data logger CR-3000 (Campbell Scientific, Canada) that also recorded data at 10 Hz.

The clock of the internal PC of the UHSAS and the laptop were not precise and showed some drift over time. In order to quantify the drift between the different clocks, times given by the data logger and the UHSAS internal PC were logged together at 10Hz onto the laptop PC, allowing precise temporal alignment of the wind and particle data. Clock synchronization was dealt with by ensuring UHSAS data had unique continuous 0.1 s timestamps, and a maximum correlation technique (see below) with the anemometer signal was used to find the precise lag. More details are given in supplementary material Appendix A.

The UHSAS response was tested every two days with an aerosol of 100 nm polystyrene latex (psl) spheres and calibrated every week with psl spheres of 100, 356, 505 and 752 nm.

1.2.1. Characterization of the experimental set-up

The experimental set-up was reproduced in the lab and the concentration response of the UHSAS compared with recently calibrated samplers: SMPS 3034 (TSI, USA) and APS 3321 (TSI, USA). The advantage of this characterisation is that we account for both the UHSAS counting efficiency and the line losses of the set-up. Ambient room air was sampled over 3 min intervals for 3 hours

(Fig. 3). The aerodynamic diameter measured by the APS was converted to a geometric diameter assuming a density of 2g.cm^{-3} and assimilating particles to perfect spheres (dynamic shape factor of 1). Under the same assumption of particle sphericity, the electrical mobility diameter is equivalent to the geometric diameter. The optical diameter measured by the UHSAS was not converted to a geometric diameter because of the lack of information on the refractive index of the particles sampled in the room. However, Cai et al. (2008) showed the UHSAS-measured optical diameter agreed within 10% with the mobility diameter detected by a SMPS for a large range of spherical and non-spherical particles. The counting efficiency of the UHSAS was then evaluated by comparison with the SMPS and the APS, as:

$$E = \frac{\left. \frac{dC}{dd_p} \right|_{\text{UHSAS}}}{\left. \frac{dC}{dd_p} \right|_{\text{SMPS}}} \quad (2)$$

A discontinuity of the UHSAS size distribution occurs around 300 nm and is related to the "stitch" performed by the instrument software between two different gain stages (Fig. 3).

The UHSAS counting efficiency is not constant throughout the fine mode, and varies from close to 0 to 0.8. The lowest efficiency occurs for the smallest and largest particles, with the window corresponding to an efficiency larger than 50 % located between 68 and 292 nm. This observation holds only for the full experimental set-up rather than the UHSAS alone and highlights the limited detection efficiency of our set-up on both ends of the size spectrum. Phenomena likely responsible for particle losses are deposition on the tube walls and elbows by Brownian diffusion and turbulent impaction as well as non-isokinetic sampling (Brockmann, 2001). The raw concentrations were modified to account for the set-up counting efficiency by taking the SMPS as reference. In the analysis, we present the results for the entire size spectrum but will focus the results of the size range 68-292 nm as we consider them more reliable.

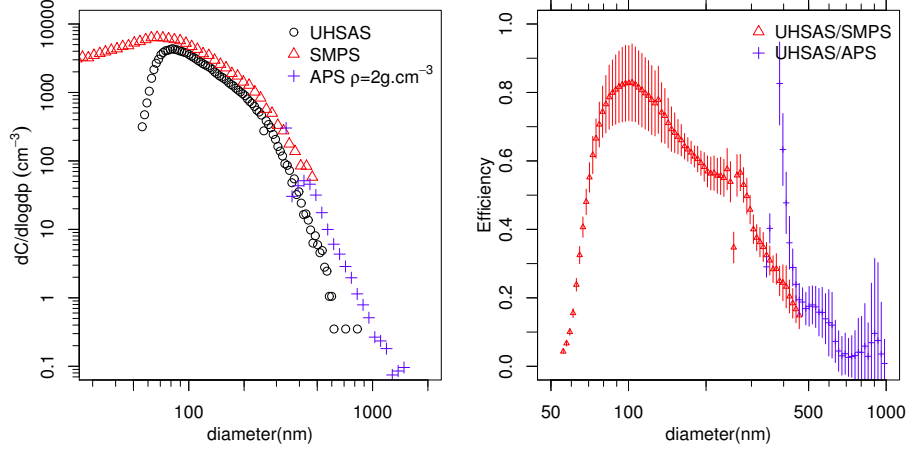


Figure 3: Counting efficiency of the UHSAS in the experimental set-up. On the left, the particle distribution measured by the UHSAS is compared with the APS and SMPS response for one particular 3 min sample. On the right, the counting efficiency of the UHSAS (Eq. 2) is evaluated over 60 samples. The symbol represents the mean and the bar one standard deviation.

1.2.2. UHSAS time response

The time response of the UHSAS to a concentration step change was evaluated in the lab. The flow switches between an atomizer flow fed with 100 nm psl spheres and a flow going through an HEPA filter. 20 replicates were performed under the "up" and "down" configurations (Fig. 4). Concentrations were normalized by the average concentration over 5 seconds. The results were fitted using a nonlinear least-squares Marquardt-Levenberg algorithm with the equations $C^+ = 1 - \exp(-(t - t_0)/\tau_{up})$ and $C_1^+ = \exp(-(t - t_0)/\tau_{down})$. In the case of the "down" configuration, a fit with a sum of exponentials was tested as well : $C_2^+ = \exp(-(t - t_0)/\tau_{down1}) + \exp(-(t - t_1)/\tau_{down2})$.

The UHSAS reacts to a concentration change with a time constant of 0.43 s in the "up" configuration. In the "down" configuration, the fit with a single exponential of time constant of 0.65 s is not quite satisfactory. When fitted with

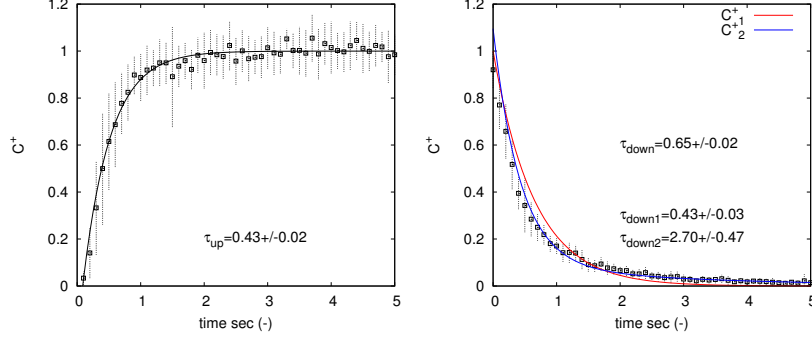


Figure 4: UHSAS time constants associated to concentration step changes

a sum of exponentials, the fit is better and indicates the same time constant
 (0.4 s) for the "fast" response with a contribution of a slower response whose
 time constant is 2.7 s. Based on that, an average time constant of 0.5 s was
 therefore adopted to characterize the response of the UHSAS and was used to
 calculate the spectral losses of the flux (see Sec. 1.4).

1.3. Flux measurements by eddy-correlation

The vertical particle number flux of size bin i was calculated as the correla-
 tion between the turbulent fluctuation c'_i of the number concentration and the
 turbulent fluctuation of the vertical wind w' : that is $\overline{c'_i w'}$, where the overbar
 refers to the Reynolds time average. The averaging period was chosen as 30
 min. The following assumptions are required for this flux to be constant above
 the canopy and to reflect the interaction of the canopy with the atmosphere :
 stationarity, incompressibility and horizontal homogeneity of the flow as well
 as the absence of creation or destruction of particles between the measurement
 height and the canopy top (for example Baldocchi et al., 1988; Kaimal and
 Finnigan, 1994). This creation or destruction of particles could be due to nucle-
 ation, condensation, evaporation, coagulation or fragmentation. Some of these
 assumptions were often not met and flux corrections were required (see Sec.
 1.5).

1.4. Flux calculations

The flux calculation was performed using the Edire software (R. Clement,
University of Edinburgh). A classical procedure was applied to the data, as
summarized by Mauder et al. (2006): Data were screened for physically non-
possible values and spikes following Vickers and Mahrt (1997). No spikes were
removed in the particle signal (as opposed to the wind data), to avoid filtering
out real signals. Signals were not detrended, in accordance with Lee et al.
(2004). The lag between the different sensors and the sonic anemometer was
calculated by maximizing the correlation between the signals. Wind coordinates
were rotated using the planar fit method (Wilczak et al., 2001). The fluctuations
of the sonic temperature were converted into fluctuations of actual temperature
for calculation of the sensible heat flux (Schotanus et al., 1983). The cross-wind
correction of the sonic temperature was performed internally by the Campbell
sonic anemometer (Schotanus et al., 1983; Liu et al., 2001).

1.5. Particle flux corrections

Flux corrections were included for spectral loss, storage term and the influence of humidity.

1.5.1. Spectral losses

Spectral losses occur at high frequency due to the slow time response of the sensors, path length averaging, sensor separation and tube attenuation (Moore, 1986; Horst, 1973; Massman, 1991). They were corrected using the method of Moore (1986), based on the empirical cospectral shapes of Kaimal et al. (1972).

The UHSAS time constant τ was determined to be 0.5 s (see Sec. 1.2.2). Over the full campaign, the correction γ_s had a median of 1.27 (25 and 75 percentiles of 1.18 and 1.30).

1.5.2. Storage term

Flux divergence can occur when the signal is not stationary over 30 min. The so-called storage term between the ground and the measurement height was evaluated as:

$$\begin{aligned} Fst_i &= \int_0^{z_R} \frac{dC_i}{dt} dz \approx \frac{d}{dt} \int_0^{z_R} C_i dz \\ &\approx z_R \frac{C_{iR}(t + \Delta t) - C_{iR}(t)}{\Delta t} \alpha_i \quad \text{with } \alpha_i = \frac{1}{z_R} \int_0^{z_R} C_i^+ dz \end{aligned} \quad (3)$$

where C_i is the average concentration in the bin i with $C_i(z, t) = C_{iR}(t)C_i^+(z)$, C_{iR} is the concentration at the measurement height and C_i^+ the non-dimensional concentration. This average concentration was calculated over 2 min at the beginning of each sample of $\Delta t = 30$ min.

The vertical profile of C_i^+ and the integral term α_i were calculated every half hour using a one-dimensional deposition model developed for broadleaf canopies (Petroff et al., 2009, see its description hereafter). For the particle bins studied here, α_i is larger 0.95, which means that the concentration is close to constant below the measurement height. This conclusion would not be true for smaller or larger particles that are more prone to deposition. The ratio of the storage term to the measured flux had a median varying between 17 and 24 %, depending on the size bin (and 22 % for the total count). Its diel contribution for each size bin is represented in Figure 5.

1.5.3. Accounting for the influence of humidity fluctuation: WPL correction

Fluxes were corrected to account for fluctuation in air moisture. The Webb-Pearman-Leuning (WPL) correction (Webb et al., 1980) is expressed as a vertical velocity $Vwpl$ defined by:

$$Vwpl = 1.61 \frac{\overline{w' \rho'_v}}{\rho_{air}} + (1 + 1.61\bar{q}) \frac{\overline{w' T'}}{\bar{T}} \quad (4)$$

where ρ_v is the water vapour density, ρ_{air} the dry air density, q the specific humidity, w the vertical wind velocity and T the air temperature. This correction is independent of the particle size and exhibits a maximum around midday of

the order of 0.5 mm.s^{-1} (Fig. 5). The second term of Eq. 4 cannot be neglected because the distance between the inlet and the particle counter is too small to assume the complete dampening of the temperature fluctuations inside the tube (Rannik et al., 1997). The second term of Eq.4 is kept, even though it could mean an overestimation of the WPL flux. The ratio of the WPL flux to the measured flux had a median varying between 3 and 8 %, depending on the size bin (and 7 % for the total count). Its diurnal evolution is given in Figure 5.

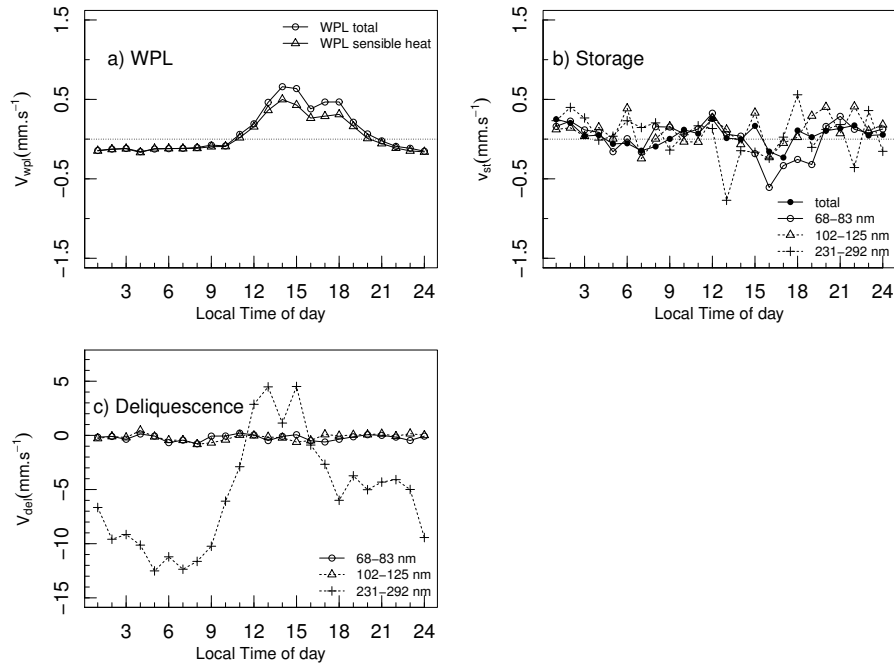


Figure 5: Diurnal cycles of the corrections of the transfer velocity: a) WPL, b) Storage, c) Deliquescence. Medians are displayed.

1.5.4. Accounting for the influence of humidity fluctuation on aerosol size: deliquescence correction

Another flux correction is often mentioned in the literature and accounts for the influence of the relative humidity fluctuation on the size distribution of

a hygroscopic aerosol (Fairall, 1984; Kowalski, 2001; Vong et al., 2004, 2010). Whether to apply this correction or not depends on the ambient conditions inside the particle counter, how much they differ from dry conditions and if the aerosol particle has time to reach its equilibrium size before being counted. In our experimental set-up, the line between the inlet and the particle counter is short (approximatively 4 m) and not heated, which means the humidity fluctuations are likely not dampened and should be accounted for. But the degree to which the particles are dried inside the instrument is unknown: depending on the authors using similar particle spectrometers, this correction is included (Vong et al., 2004, 2010) or not (Gallagher et al., 1997; Nemitz et al., 2002, 2004). Furthermore, the discussion whether to include or not this correction applies as well to other particle measurement techniques, such as condensational particle counter -it was included in (Buzorius et al., 2000) and (Pryor, 2006) but not included in (Rannik et al., 2009)-; or electrical aerosol spectrometer -it was included in (Gordon et al., 2011) and (Deventer et al., 2015) but not included in (Pryor et al., 2009)-. In the present study, we will evaluate this correction even if we are not certain of its relevance in the present set-up. Based on Fairall (1984) and simplified by others (Kowalski, 2001; Vong et al., 2004, 2010), the flux correction due to the hygroscopic growth of the particles can be expressed as a vertical velocity :

$$Vdel_i = -\beta_i \gamma \frac{\overline{w' S'}}{1 - S} \quad (5)$$

where S is the instantaneous saturation ratio (RH/100). The parameter γ depends on the hygroscopic properties of the aerosol. It appears in the parametrization of the growth factor, i.e. the ratio of the wet diameter and the dry diameter, proposed by Swietlicki et al. (2000): $d_p/d_{p0} = (1 - S)^{-\gamma}$ with d_{p0} the diameter of the dry particle. In order to give an estimate of γ , we rely on literature as well as our measures of the aerosol composition at the site. According to Meyer et al. (2009), pure ammonium sulfate droplets have a growth factor of 1.48 at $S = 0.85$, which corresponds to $\gamma = 0.2$. When there is an organic phase in the aerosol and the volume fraction increases until 0.5, the same study

shows a growth factor decreasing to 1.3 at $S = 0.85$, that is $\gamma = 0.14$. During the campaign, we measured on 15 occasions the chemical composition of the water-soluble fraction of the aerosol using a MOUDI impactor (Model 110, MSP, USA), focusing most of the time on the inorganic fraction. The fine mode of the inorganic fraction (less than $1.8\mu\text{m}$) was dominated by ammonium sulfate. On three occasions, the bulk organic carbon mass concentration was measured and the ratio PM1.8 organic/(PM1.8 organic+inorganic) is found to vary between 20 and 40 %. Other compounds than water-soluble inorganic and organic compounds can exist in the aerosol mixture that could be non hygroscopic (for example soot) or more hygroscopic. One long-term study in a Swedish rural area shows a growth factor at $S = 0.9$ varying on average throughout the year between 1.3 and 1.5 for particle dry diameter between 50 nm and 265 nm, which corresponds to $\gamma = 0.11$ and $\gamma = 0.18$ (Fors et al., 2011). Based on the literature and our chemistry measurements, we choose a constant $\gamma = 0.15$ for the present study.

The exponent β_i is defined in the Junge power-law (Junge, 1963) by $\frac{dC}{d\log d_p} \propto d_p^{-\beta_i}$. This model is a rough description of the atmospheric aerosol distribution that is only valid on limited size ranges. In this study, the exponent β_i is evaluated every half-hour for each of the 14 size bins by fitting of the 100 raw size bins (see Sec. 1.2). In order to reduce the influence of the UHSAS stitching, the size bins 188-231 nm, 231-292 nm and 292-359 nm were aggregated for the fitting. The main statistics of β_i are given in Table 1.

We were not able to calculate a deliquescence correction for the total number of particles because of our limited knowledge of the size spectrum outside of the UHSAS detection range.

Due to the high humidity experienced during this campaign (mean RH of 75 % with a strong diurnal cycle, see Fig. 8), the deliquescence correction was significant. The ratio of the deliquescence correction to the measured flux had a median varying between 28 and 190 %, depending on the size bin. Its diurnal evolution is given in Figure 5.

Given the importance of the deliquescence correction, we will distinguish

Size bin	$d_p(nm)$	β_i 25%	β_i median	β_i 75%
55-068 nm	60.94	-1.59	1.68	3.11
68-083 nm	74.81	-0.47	0.40	1.55
83-102 nm	91.84	-1.65	-1.02	-0.38
102-125 nm	112.75	-0.57	0.16	0.86
125-153 nm	138.41	-0.47	0.27	1.24
153-188 nm	169.91	0.80	1.56	2.60
188-231 nm	208.59	3.82	4.50	5.56
231-292 nm	259.84	3.85	4.52	5.56
292-359 nm	323.7	3.87	4.51	5.51
359-440 nm	397.38	4.65	5.52	6.61
440-541 nm	487.83	5.63	7.63	9.21
541-664 nm	598.87	2.33	4.22	6.65
664-815 nm	735.19	4.56	6.35	8.39
815-1000 nm	902.54	4.40	6.31	8.29

Table 1: Statistics of the factor β_i in the deliquescence correction, where d_p is the geometric mean of the size bin.

amongst results whether the latter is taken into account or not in the total flux calculation. The total flux without the deliquescence correction is expressed as $F_i = \gamma_s \overline{c'_i w'} + Fst_i + Vwpl.C_i$ while the total flux accounting for the deliquescence correction is expressed as $Fdel_i = \gamma_s \overline{c'_i w'} + Fst_i + (Vwpl + Vdel_i) C_i$. Transfer velocities are introduced as convenient parameters that integrate the influence of the properties of the canopy, the flow and the aerosol concentrations: $Vt_i = F_i / \overline{c_i}$ without deliquescence correction and $Vtdel_i = Fdel_i / \overline{c_i}$ with deliquescence correction. The sign conventions of flux apply to transfer velocity, which means that negative transfer velocity corresponds to a deposition flux (toward the forest) while a positive transfer velocity corresponds to an emission flux.

270 *1.6. Quality control*

We applied the quality control process proposed in (Foken et al., 2004; Mauder et al., 2006). Flags ranging from 1 to 9 were calculated on the following criteria: 1. stationarity of the particle flux signal, 2. fully developed turbulence, 3. wind direction with respect to the sonic orientation. The flags 1 to 3 correspond to the best quality and are used to compute ensemble averages and medians of the fluxes and transfer velocity. The data with flags from 4 to 6 can be included in the plotting of the data for trend identification. Data with flags larger than 7 are discarded. The details of the criteria used for assessing the signal quality are given in supplementary material Appendix B.

280 Examining the influence of the wind direction on the signal quality allows us to flag the influence of the tower and its wake, because no signals of quality between 1 and 6 are found in the wind sector $[10; 60]$ and a very limited number between 60 and 70 (Fig. 6). The quality control process flagged also most of the

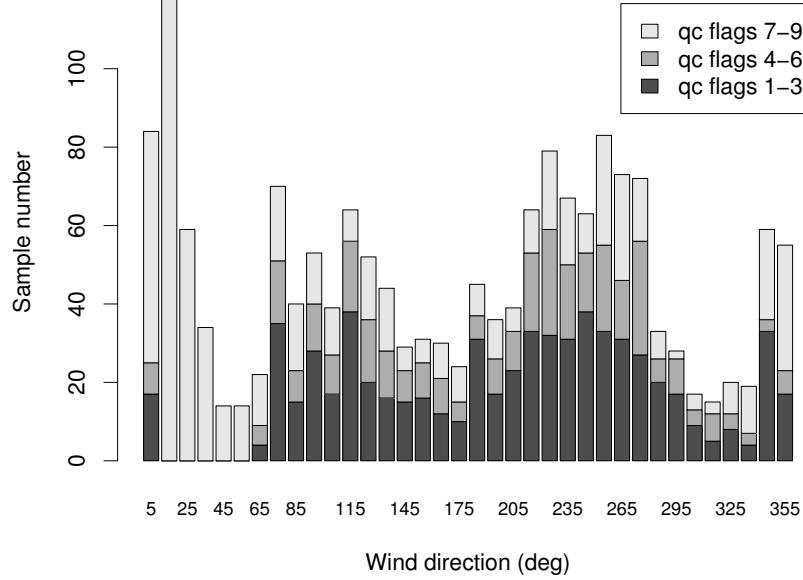


Figure 6: Influence of the wind direction of the signal quality

low-wind conditions that might have lead to contamination from the diesel generator, irrespective of wind direction: 85 % of the samples with $u_* < 0.1 \text{ m.s}^{-1}$ were given a flag larger than 3.

1.7. Particle flux uncertainties

We examine two sources of flux uncertainty, one pertaining to the counting of discrete particles, the other pertaining to the measurement of a covariance. The flux uncertainty $\Delta F n_i$ due to number counting uncertainty (for example Fairall, 1984; Nemitz et al., 2008) can be expressed as :

$$\Delta F n_i = \sigma_w C_i / \sqrt{N_i}, \quad (6)$$

where N_i is the cumulative number of particles counted in the bin i during the half hour period.

The second source of uncertainty is related to the measurement of the covariance between the vertical wind and the particle counts. Following Wyngaard (1973), the uncertainty $\Delta F cov_i$ is expressed as:

$$\Delta F cov_i = \sigma_w \sigma_{C_i} \sqrt{\tau_t / \Delta t}, \quad (7)$$

where τ_t is the integral time scale, which, following Rannik et al. (2009), can be expressed as $\tau_t = \frac{1}{2\pi\eta_t} \frac{z_R - d}{U}$ with $\eta_t = 0.21 (1 + 3.4\xi^{0.26})$ for stable conditions and $\eta_t = 0.21$ for unstable conditions and $\xi = (z_R - d)/L_O$ the stability parameter with L_O being the Obukhov length. For this campaign, the median and interquartile range of τ_t are 1.82 s [1.38; 4.07]. The main statistics of these uncertainties are given in Table 2.

In this clean environment (median particle total concentration of 2116 cm^{-3} over the campaign), the main uncertainty was related to the counting of discrete particles. Nonetheless, a significant proportion of the fluxes was greater than the uncertainty: for the total particle number and for particles smaller than 300 nm, there were more than 74% of all fluxes that were greater than the uncertainty and more than 54% of all fluxes that were greater than twice the uncertainty. The latter means fluxes are different from 0 with a 95% confidence.

size bins	$\Delta F n_i / \overline{c'_i w'} \text{ (%)}$				$\Delta F cov_i / \overline{c'_i w'} \text{ (%)}$			
	Mean	25%	Median	75%	mean	25%	Median	75%
total count	22.4	5.9	12.5	24.0	3.7	1.1	2.1	3.9
055-068nm	16.2	4.5	10.2	17.9	4.7	1.7	2.9	5.4
068-083nm	40.3	8.3	21.3	43.0	4.6	1.5	2.6	4.6
083-102nm	77.3	12.4	33.3	65.3	5.1	1.3	2.4	4.4
102-125nm	67.2	17.1	40.3	79.1	4.3	1.5	2.8	5.0
125-153nm	73.1	18.1	43.6	78.3	5.0	1.7	3.0	5.4
153-188nm	72.6	17.8	43.1	74.2	4.9	1.8	3.0	5.2
188-231nm	67.7	20.0	44.6	84.1	5.1	1.9	3.1	5.7
231-292nm	75.5	18.0	42.6	76.8	5.9	1.9	3.3	5.6
292-359nm	82.8	35.6	55.9	92.8	6.7	2.5	4.3	7.8
359-440nm	76.5	30.3	50.7	86.0	7.5	2.8	4.8	8.5
440-541nm	67.7	28.8	42.4	69.9	7.8	3.2	4.9	8.5
541-664nm	55.5	23.8	35.7	60.4	8.6	3.3	5.3	9.2
664-815nm	30.0	13.3	20.0	33.2	8.1	3.4	5.7	9.4
815-1000nm	33.4	13.2	21.3	37.3	8.3	3.3	5.3	8.9

Table 2: Uncertainty statistics related to discrete particle counting and randomness. The greyed lines correspond to size bins which detection efficiency by the UHSAS falls below 50%.

This ratio drops down to 44 % for larger particles and might be connected to the poorer counting efficiency of our setup above 300 nm and the discontinuous nature of the aerosol phase sampled at such a fast rate. Further in the paper, we will restrict the analysis on fluxes that are larger than the counting uncertainty.

305 1.8. Power spectra and cospectra

The study of power spectra and cospectra is a useful tool to evaluate the importance of noise in the signal and the ability of the different sensors to capture part or all of the atmospheric turbulence frequencies. Power spectra of the scalar x and cospectra of this scalar with vertical wind are noted S_x 310 and $C_{w,x}$. The non-dimensional frequency f is defined by $f = n.(z_R - d)/\overline{u_R}$

where n is the natural frequency. Power spectra and cospectra are made non-dimensional by multiplying them respectively with f/σ_x^2 and by $f/\overline{w'.x'}$, where σ_x^2 is the variance of the scalar x and $\overline{w'.x'}$ is the covariance between w and x . The spectra and cospectra displayed on Figure 7 were averaged over 5 successive
315 frequencies and correspond to the horizontal wind u , the concentration of CO_2 and the total number of particles C_{tot} .

In the inertial sub-range of the turbulence, Kolmogorov’s model predicts decays of the non-dimensional power spectra and cospectra following respectively a -2/3 slope and a -4/3 slope (Kolmogorov, 1941). The spectra and cospectra
320 displayed here follow these predicted trends though some white noise (slope of 1) appears in the particle channel at high frequencies ($f \approx 5 - 10$). Such white noise, often reported in particle flux studies (Ahlm et al., 2009), is not identified in the cospectra. The spectra of the horizontal wind exhibited high-frequency noise as well, which was not systematically detected in the samples.
325 Its source could be random behavior in the natural turbulent environment, high noise-to-signal ratio, aliased data outside the Nyquist cutoff frequency, effects of block averaging, or some combination thereof (Loescher et al., 2005; Kaimal and Finnigan, 1994, chap. 7).

1.9. Model description

330 A model of aerosol deposition to vegetation (Petroff et al., 2009) was used to interpret the results and evaluate if the fluxes can be explained by deposition alone. It is a stationary one-dimensional model that solves the particles’ conservation equation for each size bin. No particle-particle interactions (coagulation, fragmentation), nor gas-particle interactions (condensation, evaporation), nor
335 chemical reactions are accounted for. It is thus assumed particle number is only affected by the presence of collecting leaves. Depending on the particle size, the collection can occur by Brownian diffusion, interception, inertial impaction and turbulent impaction (sometimes referred to as turbophoresis), as well as sedimentation. No rebound or resuspension is parameterized. The reader is
340 referred to (Petroff et al., 2009) for details.

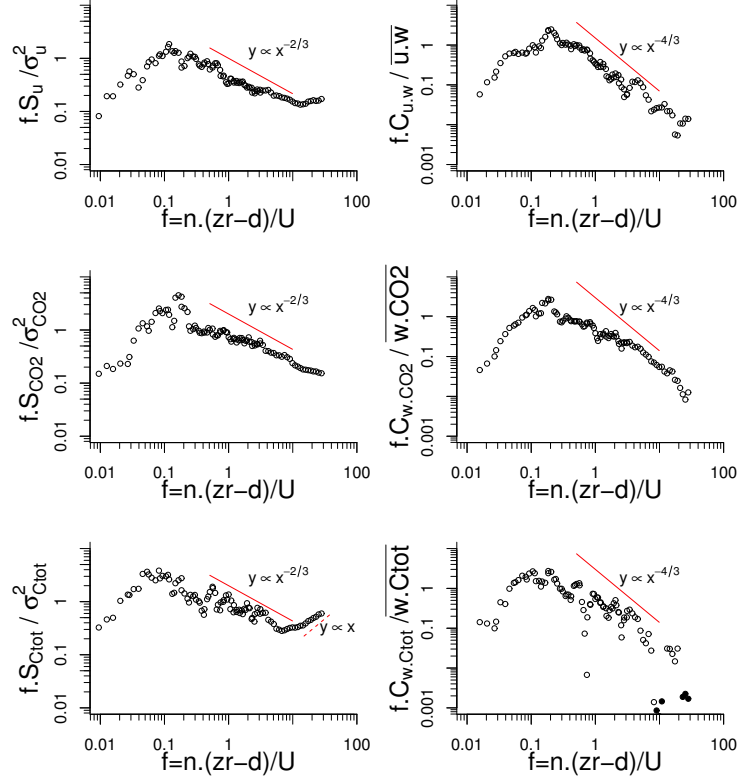


Figure 7: Typical power spectra and cospectra obtained on August, 29th, 2011 at 2.45am ($u_* = 0.36 \text{ m.s}^{-1}$, $\xi = 0.16$). Open symbols indicate positive values and closed symbols indicate for negative values.

The meteorological parameters needed by the model, such as the temperature, the sensible heat flux, the friction velocity, were measured on-site. The roughness length and displacement height are $z_O = 1.5$ m and $d = 16.5$ m. The vegetation parameters used for simulation are the following : LAI was measured on-site every 2 weeks. The vertical profile of the leaf area density is of Gaussian shape with a standard deviation depending on the trunk height $h_{tr} = 7.2$ m and the canopy height $h = 22$ m (Halldin, 1985). The distribution of the leaf inclination is plagiphile, in accordance with on-site measurements on Sugar maple

(Thomas and Winner, 2000; Nock et al., 2008). The distribution of the leaf
350 azimuth is uniform.

The choice of a characteristic dimension of the leaf is somewhat arbitrary for two reasons. First, deposition processes are modelled on rigid obstacles of rectangular shape, whose dimension perpendicular to the flow is large enough to neglect the boundary effects. For real leaves with more complex shapes and the
355 process of diffusion, Parkhurst et al. (1968) estimated the characteristic dimension to be typically between 0.5 and 0.8 of the maximum leaf width. Secondly, the stand contains multiple species with very distinct leaf shape: The two main species (Sugar maple and American beech) represent about 95% of the leaves collected in the litter traps. Sugar maple leaves have five palmate lobes and are
360 approximately as long as wide. Their leaf width can in a first approximation be estimated as the square root of the measured leaf area and the characteristic dimension is chosen as 0.6 leaf width (Parkhurst et al., 1968). Based on on-site measurements, this dimension is $L = 4.0 \pm 0.9$ cm for Sugar maple. American Beech has oval leaves whose shape is approximated by an ellipse (ratio of axis
365 $\simeq 2/5$). Its width is chosen as the minor axis and the characteristic dimension is again chosen as 0.6 leaf width. Based on on-site measurements, this dimension is $L = 2.4 \pm 0.4$ cm for American beech. For the modelling exercise, a characteristic dimension of $L = 3$ cm is chosen.

2. Observations

370 Out of the 2832 30 min observations available to us, 30 % of the signal was removed because of poor meteorological quality (too many spikes or physically non-possible data) or rain. Depending on the particle bin, between 8 and 36 % were further removed (15 % for the total count) because of missing data or large counting uncertainty (see Sec. 1.7). Valid periods with quality flags between 1
375 and 3 amount to between 479 and 759 observations (669 for the total counts) and about 360 for quality flags between 4 and 6.

The Northern sector ($\pm 45^\circ$) was excluded from the analysis because of the likely

contamination of the diesel generator located 70 m to the north of the tower.

2.1. Meteorological conditions

380 Meteorological conditions during the eight campaign weeks from August 16th, 2011 to October 10th, 2011 are displayed on Figure 8. Conditions were characterized by a high saturation ratio S (the relative humidity divided by 100), which peaked in the morning around 10 am. Around this time, the solar radiation (and the measured Photosynthetically Active Radiation-PAR) started to increase and contributed to the evaporation of the liquid water content of the atmosphere. 385 The resulting latent heat flux was of the same order as the sensible heat flux. The daytime condition was also marked by the destruction of the nocturnal boundary layer and the development of shear stress turbulence, visible here in the increase of u_* .

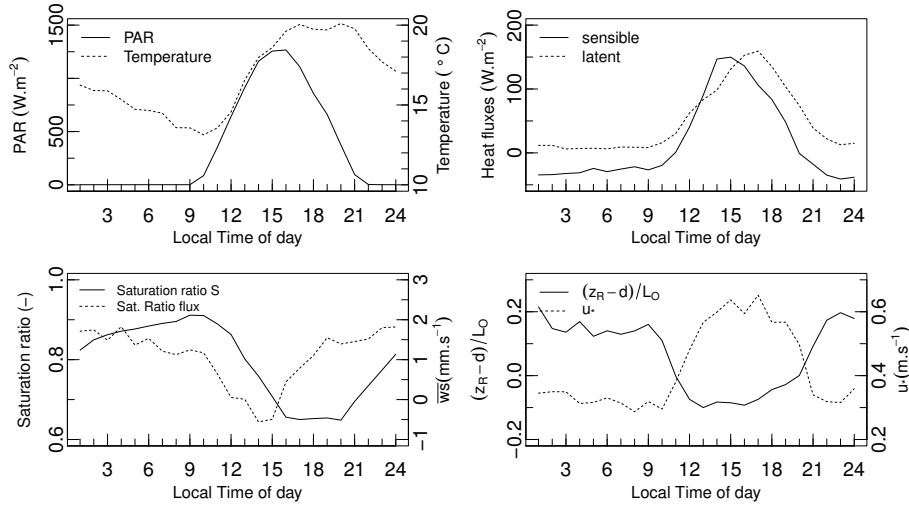


Figure 8: Diurnal cycles of the meteorological parameters. Median values are represented here.

The median of the total number concentration varied with the wind sector between 1648 and 2515 cm^{-3} , the southern being the most concentrated due to a larger population and industry concentration. (Tab. 3). Diel evolution of the

Size bin	Sample number				Median concentration (cm^{-3})				Median transfer velocity (mm.s^{-1})			
	E	N	S	W	E	N	S	W	E	N	S	W
total count	166	81	180	225	1648	1324	2515	2107	0.96	5.62	-0.51	-0.20
55-068 nm	184	89	197	261	237	198	446	337	4.11	13.36	1.11	1.97
68-083 nm	158	78	178	227	198	206	346	295	1.83	10.25	0.83	1.34
83-102 nm	126	76	135	180	219	212	387	349	0.89	5.49	-0.09	1.00
102-125 nm	109	66	125	171	221	172	419	401	0.58	2.66	-0.67	-0.27
125-153 nm	105	58	144	184	202	156	364	336	-0.37	0.88	-0.99	-0.84
153-188nm	118	42	150	186	217	109	322	228	-0.41	-1.47	-1.60	-1.45
188-231 nm	121	39	147	178	122	46	144	108	-1.89	-1.67	-2.31	-2.11
231-292 nm	112	46	137	197	86	25	123	64	0.53	-2.42	-2.94	-3.51
292-359 nm	131	52	140	195	10	3	15	7	-3.24	-4.35	-3.85	-7.35
359-440 nm	152	60	147	207	8	3	12	7	-4.34	1.15	-6.17	-5.98
440-541 nm	164	71	168	238	3	1	3	2	-8.05	-9.75	-13.24	-7.73
541-664 nm	153	64	193	237	1	0	1	1	-21.03	-29.92	13.72	19.12
664-815 nm	124	43	123	187	1	0	0	1	38.17	29.73	37.45	33.86
815-1000 nm	95	29	79	145	0	0	0	0	74.23	-35.10	-43.84	20.37

Table 3: Influence of the wind sectors on concentration and transfer velocity for signals with quality flag between 1 and 3. The greyed lines correspond to size bins which detection efficiency by the UHSAS falls below 50% and the northern sector contaminated by the generator.

particle size number concentration is shown for four days, between August, 30th and September, 3rd (Fig. 9). Two modes were visible in the particle number distribution, corresponding to the Aitken mode (diameter smaller than about 100 nm) and the accumulation mode (between 100 and 1000 nm). Growth of nucleating particles was suspected on a number of occasions, such as the morning of August, 30th, but was not investigated further in the scope of this paper. The

400 occurrence of stitches between different electrical gains of the UHSAS was visible here at 90, 200 and 300 nm.

Diel concentration cycle for the total count showed slightly more particles

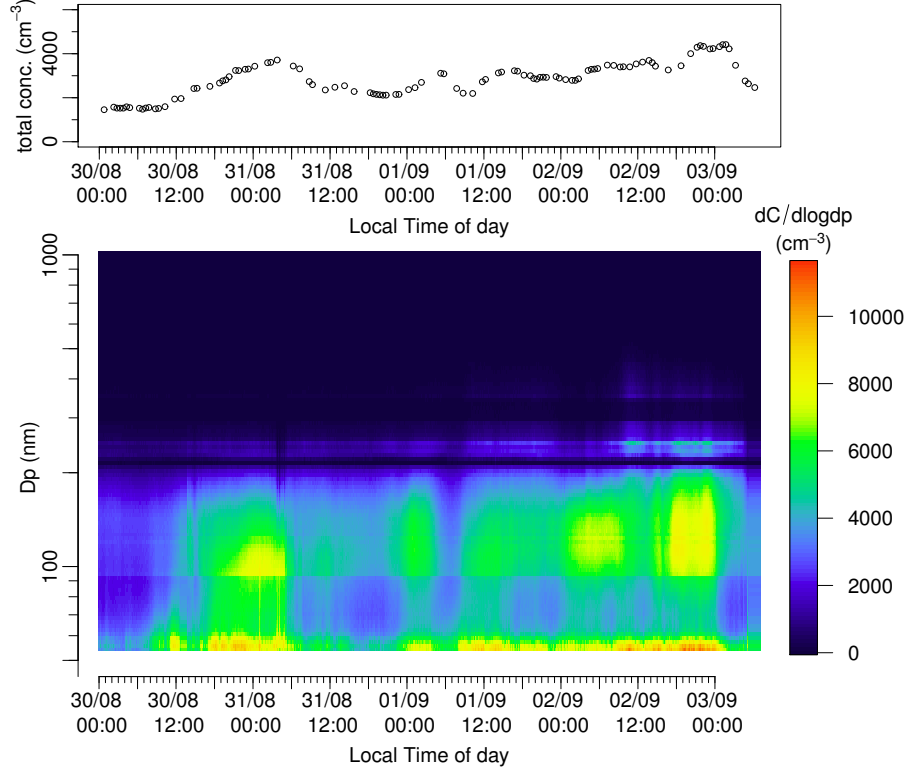


Figure 9: Diurnal variation of the total number concentration (upper panel) and the number size distribution between August, 30th and September, 3rd.

at night, possibly corresponding to the accumulation of particles in the low nocturnal boundary layer (Fig. 10).

405 2.3. Fluxes and bi-directionality

Over the campaign, the median flux of particles was $-40.5 \text{ cm}^{-2}.\text{s}^{-1}$, corresponding to a net deposition and a transfer velocity of $-0.21 \text{ mm}.\text{s}^{-1}$. The median fluxes of the first three size bins (below 102 nm) were positive, while

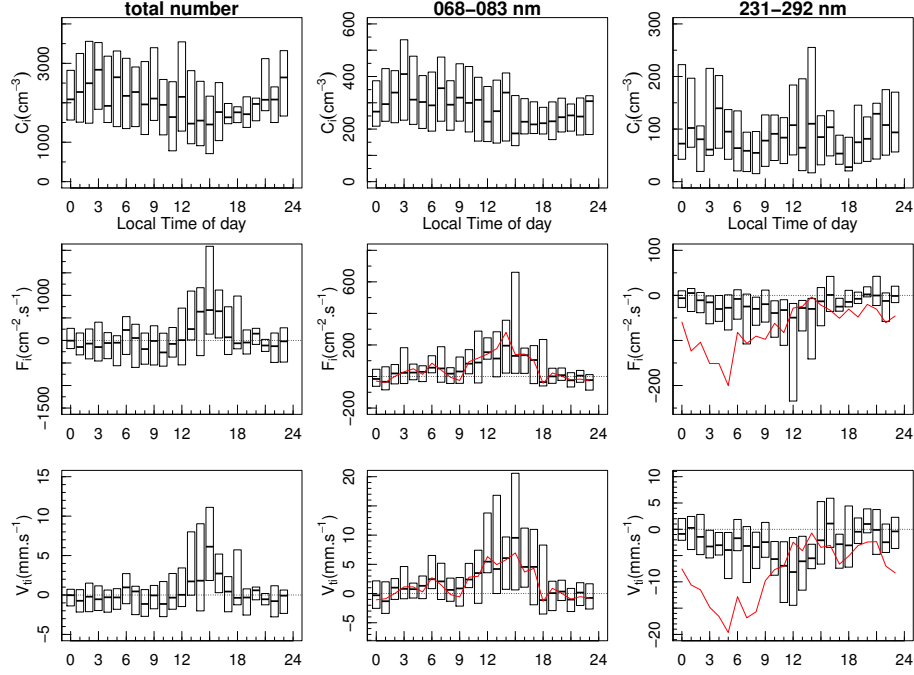


Figure 10: Diurnal variation of the concentrations, fluxes and transfer velocity for the total count (left), the 68–83 nm bin (center) and the 231–292 nm bin (right), where the horizontal bar and box represent the median and the 25, 75 percentiles without deliquescence correction, while the red line corresponds to the median of the flux and transfer velocity with the deliquescence correction.

the other bins displayed negative median flux (Tab. 4).

410 The diel evolution of the flux was different for particles smaller than 100 nm and those larger. Fluxes of smaller particles exhibited a diurnal pattern of increasing emission until about 2pm followed by a decrease till about 7pm. At night, their fluxes were close to zero. Fluxes of larger particles were consistently negative (deposition) throughout the day, this deposition reaching a maximum
415 around noon (Fig. 10).

All size bins showed bi-directional fluxes: The proportion r_+ of positive flux was 47 % for the total particle number, between 56 and 59 % for particles smaller

Size bin	d_p (nm)	Nb	F_i 25%	F_i 50%	F_i 75%	r_+	$Fdel_i$ 25%	$Fdel_i$ 50%	$Fdel_i$ 75%	r_+
total count	NA	669	-383.6	-40.5	340.1	47.1	NA	NA	NA	NA
55-068nm	60.94	759	-151.9	65.1	261.8	56.5	-309.9	-27.1	223.3	46.5
68-083nm	74.81	664	-45.5	35.7	130.5	59.2	-58.6	22.4	134.5	57.2
83-102nm	91.84	513	-31.5	20.2	89.4	56.7	-12.5	45.1	184.3	68.7
102-125nm	112.75	479	-47.7	-11.8	48.6	44.3	-68.7	-10.2	56.7	45.5
125-153nm	138.41	500	-66.3	-20.8	26.6	37.6	-102.9	-26.7	30.7	38.5
153-188nm	169.91	537	-76.8	-29.2	14	29.8	-186.4	-64.3	-8.5	22.0
188-231nm	208.59	521	-58.5	-20.0	7.8	26.9	-220.1	-76.4	-20.0	15.0
231-292nm	259.84	527	-60.0	-16.4	9.0	33.4	-153.4	-59.2	-8.1	16.8
292-359nm	323.7	563	-11.8	-2.9	5.1	39.8	-22.3	-6.3	1.8	30.7
359-440nm	397.38	595	-13.1	-3.4	6.1	39.5	-24.7	-7.7	1.5	29.8
440-541nm	487.83	678	-6.7	-1.7	5.2	44.1	-11.1	-3.1	2.5	34.3
541-664nm	598.87	695	-3.4	0.7	3.7	51.4	-4.1	0.3	3.4	49.9
664-815nm	735.19	518	-5.5	2.1	7.1	56.4	-6.6	1.3	6.8	55.4
815-1000nm	902.54	374	-4.4	1.3	5.1	53.7	-4.9	1.0	4.9	53.2

Table 4: Particle flux statistics. The median, 25 percentile et 75 percentile of the flux ($\#.cm^{-2}.s^{-1}$) as well as the proportion of positive flux r_+ are given whether the deliquescence correction is accounted for or not (respectively F_i and $Fdel_i$). Only signals of quality between 1 and 3 are considered and the northern sector is excluded. The greyed lines correspond to size bins which detection efficiency by the UHSAS falls below 50%. Nb is the number of valid samples.

than 102 nm, while particles larger than 102 nm exhibit an r_+ between 27 and 44 % (Tab. 4).

Accounting for the deliquescence correction did not change the fact that there is a majority of positive fluxes for particles smaller than 102 nm. It rather changed r_+ to 57 and 69% respectively for 68-83 nm and 83-102 nm bins. For particles larger than 102 nm, accounting for the deliquescence correction led to a significant increase of downward fluxes, particularly between midnight and 9 am due to high humidity flux and humidity (Fig. 8), and a decrease of r_+ to a value between 15 and 45 % depending on the size bins. The deliquescence

correction is about one order of magnitude higher for the 231-292 nm bin than the 68-83 nm bin due to the value of the β factor (Tab. 1).

The proportion of positive fluxes varied throughout the day as well. We focused
 430 on the total number of particles and on the three following size bins: 68-83 nm typical of apparent emission, 102-125 nm, 231-292 nm typical of apparent deposition (Fig. 11). A distinct diel cycle of r_+ was observed: the Aitken mode particles (68-83 nm) were preferentially emitted throughout the day, with a maximum of $r_+ = 85\%$ in the afternoon, while the fine mode particles (231-292 nm)
 435 were preferentially deposited throughout the day, with a minimum $r_+ = 18\%$ in the morning. For the total count, the proportion of positive flux remained between 40 and 50 % for most of the day, except in the late afternoon when it increased to 70 %.

Accounting for the deliquescence correction modified the diurnal evolution of r_+
 440 throughout the spectrum. The proportion of positive flux of the Aitken mode particles (68-83 nm) was much larger in the afternoon, peaking at 89 % at noon, while the fine mode particles (231-292 nm) were depositing more consistently in the early morning ($r_+ = 0$ at 6am).

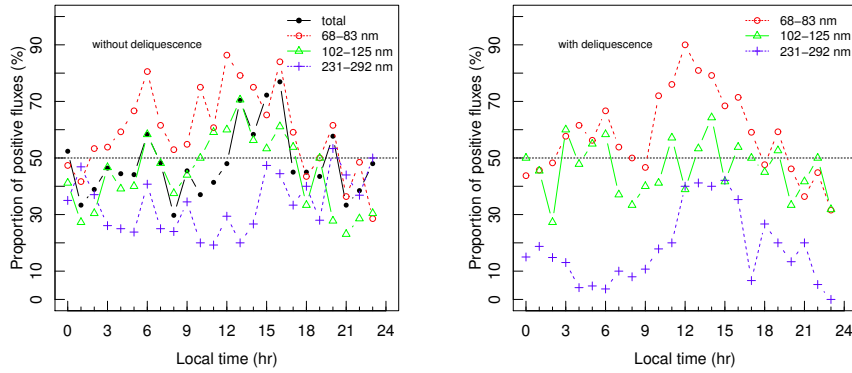


Figure 11: Diurnal variation of the proportion of positive fluxes, without the deliquescence correction (left) and with the deliquescence correction (right).

2.4. Transfer velocity

445 For the reliably detected size bins (68-292 nm), median transfer velocity for each size bin ranged from $+1.34$ to -2.69 mm.s^{-1} (Tab. 5). Its diel evolution over three consecutive days (Fig. 12) emphasized the opposite behaviour of particles smaller than about 100 nm versus those bigger. Highest deposition occurred for particles of 231-292 between 10am and noon while highest emission

450 of finer particles occurred later in the afternoon between 1 and 3pm.

These three days were characterized by larger concentrations and higher geo-

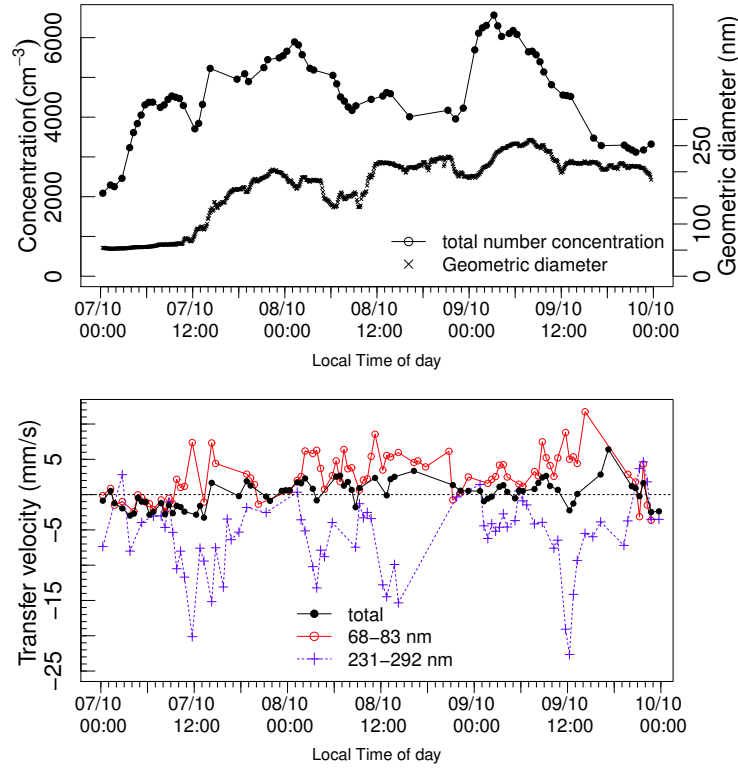


Figure 12: Evolution of total concentration, geometric diameter and transfer velocity over 3 days. For clarity sake, transfer velocity are shown only without accounting for deliquescence.

metric diameter. Evidence from NO_x/NO_y signals as well as continental plume

detection were consistent with large smoke plumes from forest fires coming from the West/South-West (see Geddes and Murphy, 2014, for further details).

455 The main statistics of the transfer velocity over the measurement campaign are given in Table 5. Also given are the medians of the modelled transfer velocity, calculated with on-site meteorology and leaf area index (see section 1.9 for the other parameters). Contrary to the model, the measurements (without deliquescence correction) did not display a minimum of deposition between 200 and 300
460 nm, but rather a constant decrease of the transfer velocity when the diameter increased, from a positive median value of $+1.34 \text{ mm.s}^{-1}$ for the 68-83 nm bin (emission) to a negative median value of -2.69 mm.s^{-1} for the 231-292 nm bin. For diameter larger than 125 nm, the measured decrease of the transfer velocity (corresponding to an increase of the deposition rate) was much stronger than
465 predicted by the model. This discrepancy will be investigated in the discussion section.

3. Discussion

3.1. Occurrence of positive fluxes

Prior studies have reported a proportion of upward particle fluxes from forest ecosystems as well: With a CPC 3010 (TSI, USA), the reported proportion
470 of upward fluxes ranged from 30 to 40% (Ahlm et al., 2009; Rannik et al., 2003; Pryor et al., 2007). With the FMPS (TSI, USA), the range went from 30% (Pryor et al., 2009) to 60% (Gordon et al., 2011). With an optical counter, Vong et al. (2010) reported upward fluxes in the accumulation mode but gave
475 few details about their importance and recurrence. Recently, Deventer et al. (2015) used an electrical aerosol spectrometer to measure forest fluxes of particles between 10nm and $1 \mu\text{m}$ and found a r_+ to vary between 20% and 52 % without deliquescence correction, this maximum being reached for particles of 70 nm diameter, similar to the present study.

480 Multiple explanations have been given in the literature to explain the common occurrence of upward fluxes. Some of the proposed explanations can be tested

Size bin	Vt_i 25%	Vt_i 50%	Vt_i 75%	$Vtdel_i$ 25%	$Vtdel_i$ 50%	$Vtdel_i$ 75%	$Vtmod_i$ 50%
total count	-1.95	-0.21	1.7	NA	NA	NA	NA
55-068 nm	-4.56	2.12	7.39	-8.48	-0.7	7.34	-0.40
68-083 nm	-1.78	1.34	4.83	-2.48	0.85	4.96	-0.32
83-102 nm	-1.20	0.71	3.25	-0.44	1.93	5.63	-0.25
102-125 nm	-1.71	-0.47	1.65	-2.63	-0.46	2.16	-0.21
125-153 nm	-2.39	-0.86	1.06	-3.91	-1.12	1.34	-0.18
153-188 nm	-2.95	-1.45	0.64	-7.24	-2.91	-0.39	-0.16
188-231 nm	-4.86	-2.17	0.55	-15.74	-8.36	-2.00	-0.15
231-292 nm	-6.40	-2.69	1.83	-16.81	-8.18	-1.91	-0.15
292-359 nm	-12.52	-4.70	8.36	-22.49	-9.40	3.48	-0.15
359-440 nm	-15.27	-6.14	10.44	-27.46	-12.40	3.25	-0.16
440-541 nm	-30.60	-9.37	21.84	-45.59	-17.04	14.20	-0.19
541-664 nm	-53.46	13.54	56.46	-56.04	5.04	45.33	-0.23
664-815 nm	-77.28	33.80	118.53	-76.97	21.54	92.09	-0.26
815-1000 nm	-149.49	39.70	161.79	-161.36	30.65	142.00	-0.31

Table 5: Particle transfer velocity. The median, 25 percentile et 75 percentile of the transfer velocity (mm.s^{-1}) are given with and without the deliquescence correction (respectively Vt_i and $Vtdel_i$). The median of the modelled transfer $Vtmod_i$ is calculated with the parameters given in the text. The greyed lines correspond to size bins which detection efficiency by the UHSAS falls below 50%.

on the present measurement campaign. Other, because of the absence of simultaneous measurements in the present study, are only mentioned.

Upward fluxes due to the evolution of the aerosol size distribution. The number concentration of particles in a specific size bin is not a conservative scalar. It can be altered between the altitude of measurement and the canopy by interactions occurring between particles (coagulation, agglomeration, fragmentation), between particles and the carrying gas (mass transfer of water vapour), by chemical reactions (condensation of biogenic volatile organic compound BVOC or evaporation of secondary organic aerosol SOA).

Recent measurements involving Aerosol Mass Spectrometry gave some insights

in these complex and highly variable dynamics (Nemitz et al., 2008; Gordon et al., 2011; Farmer et al., 2015). Farmer et al. (2015) observed on a temperate broadleaf forest predominantly upward fluxes of organic aerosols, while the flux of sulphates were predominantly downwards. The authors hypothesize that the upward flux was due to the rapid oxidation of BVOC and growth of freshly nucleated SOA. This led to an accumulation of SOA inside the canopy that was later ejected to the upper canopy and cause an emission flux. They also suggested that this upward flux was in some instances stronger than the deposition of older more oxidized organic aerosols. Such processes could explain the apparent emission in the sub-100 nm size range observed in the present campaign. The existence of a thermal gradient between the inner canopy and the atmosphere has been suspected to alter the partitioning of semi-volatile compounds between the liquid aerosol phase in the form of ammonium nitrate, and the vapour phase in the form of ammonia and nitric acid (Nemitz et al., 2004; Farmer et al., 2011). In the present campaign, the fine mode was dominated by ammonium sulfate, which partitions irreversibly to particle phase. An alteration of the liquid-gas partitioning is thus unlikely to participate to these apparent upward fluxes.

Upward fluxes due to an ill-characterized deliquescence correction. A strong uncertainty persisted in the evaluation of the deliquescence correction, which is important enough to change a positive flux into a negative flux. Three aspects of this correction carried uncertainty:

First, it is not known how the particle size was modified by humidity fluctuations inside the measurement apparatus, whether in sampling line or inside the laser chamber: Were the humidity turbulent fluctuations partially or fully dampened ? Were the particles partially or fully dried inside the particle counter ?

Second, we relied on the UHSAS for measuring both the particle fluxes and the particle size distribution. Because of the limited detection efficiency of the UHSAS and our set-up for particles smaller than 68 nm and larger than 292 nm, we might not evaluate adequately the factor β intervening in the Junge Power

law. The correction could imply a change of sign in the fluxes below 100 nm.

Third, there is a conceptual uncertainty in the formulation of the correction itself, because of the use of the Junge Power law, known to misrepresent a realistic multi-modal size distribution. To somewhat balance that, the Power law was fitted locally on each size bin. Moreover, the expression of the particle growth was simplified in order to only depend on the relative humidity (Swietlicki et al., 2000). Though very convenient, this formulation is an empirical fitting that might not capture the full complexity of the deliquescence process.

In order to avoid such uncertainty in future measurement campaigns, one should consider adding a constant humidity chamber ahead of the counter (as proposed by Farmer et al., 2015), control that the size equilibrium time scale is smaller than the transport time scale through the measurement apparatus, and evaluate the level of drying occurring inside the sampler.

3.2. Drivers of particle deposition

3.2.1. Transfer velocity and particle size

Particle size is one main driver of transfer velocity, as the physical processes affecting the deposition are a function of particle size (Brownian diffusion, interception, inertial and turbulent impaction and sedimentation). A comparison with other measurement campaigns is given on Figure 13 in terms of the ratio of transfer velocity to friction velocity. Elements of comparison are recent measurements over both coniferous and broadleaf forests involving size-segregated particle measurements. One exception is the Hyytiälä long-term aerosol study (Mammarella et al., 2011) that relies on a CPC to measure the aerosol bulk number flux and a DMPS to estimate a geometric mean diameter. For the sake of clarity, only the median values are represented. The results of the model for broadleaf and coniferous forests were also displayed on Figure 13 . It should be emphasized that these campaigns use different measurement techniques and that the corresponding definition of the diameter is not the same : electrical mobility diameter (Mammarella et al., 2011; Pryor et al., 2009; Gordon et al., 2011), aerodynamic diameter (Deventer et al., 2015), optical diameter

(this study). However, no attempt was made to convert the diameters because of the lack of information about particle shape, dynamic factor and refractive index.

Apart from Gordon et al. (2011) and the smallest particle bins of the present

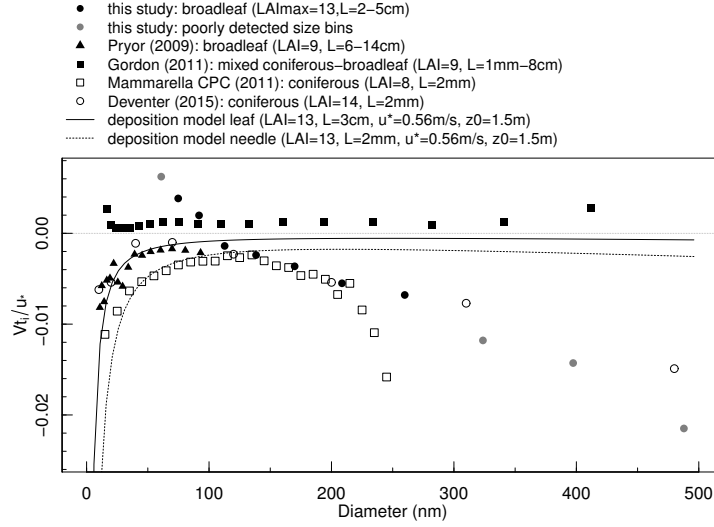


Figure 13: Evolution of the non-dimensional transfer velocity with the particle diameter. Symbols correspond to the medians. The main parameters of the model are given in the legend. Other relevant parameters are representative of the present campaign: crown base height=7.2 m, canopy height=22 m, $d=16.5$ m, $T_{pe}=16.3$ °C, $H=-10$ W.m⁻², $\rho_p=2000$ kg.m⁻³.

555

study, all campaigns displayed overall negative transfer, meaning that there was more downward than upward fluxes. Focusing on the negative data, the range of variations among the different campaigns for a given diameter was small. The CPC long-term campaign departed from other results above 200 nm. It might be linked to the fact that measured bulk number fluxes did not correspond to a single-mode size distribution (and one geometrical diameter) but rather to a multi-modal distribution (Held et al., 2006). When we only consider size bins above 102 nm, the present measurements are consistent with other measure-

560

ments on broadleaf and coniferous forests, even when the poorly-detected size
565 bins above 300 nm were included.

According to theory, the size of the individual obstacles (leaves or needles) is
affecting the aerosol deposition: the smaller the obstacle, the greater the depo-
sition per surface unit is. This is true for all processes involved in the deposition
of Aitken and accumulation mode particles, such as Brownian diffusion, inter-
570 ception and impaction. This influence was visible in the model results and
corroborated by two measurement sets (Pryor et al., 2009; Mammarella et al.,
2011). The third one (Deventer et al., 2015) was obtained on a coniferous forest
and did not display a significant difference from the broadleaf campaign, even
though the obstacle size is much smaller and the leaf area index larger. Such
575 inconsistency might be explained at least partially by the variation range of the
measurements around the medians.

The model was generally consistent with measurements of particles in the Aitken
mode ($d_p < 100\text{nm}$) but seemed to depart quite significantly for particles in the
accumulation mode. Further measurements should corroborate that. We sus-
580 pect there might be other physical processes enhancing particles collection by
leaves, such as leaf fluttering or micro-roughness interception.

3.2.2. *Transfer velocity and friction velocity*

Friction velocity is a convenient proxy for turbulence mixing. For particle
bins consistently depositing (188-231 nm, 231-292 nm) and for particle bins
585 consistently emitting (68-83 nm, 83-102 nm), the increase of friction velocity
corresponded to an increase of the transfer, whether it was positive (emission)
or negative (deposition) (Fig. 14). Other size bins as well as the total particle
counts exhibited a non-monotonic dependence on friction velocity. It likely re-
flected the coexistence of processes responsible for both emission and deposition.

590

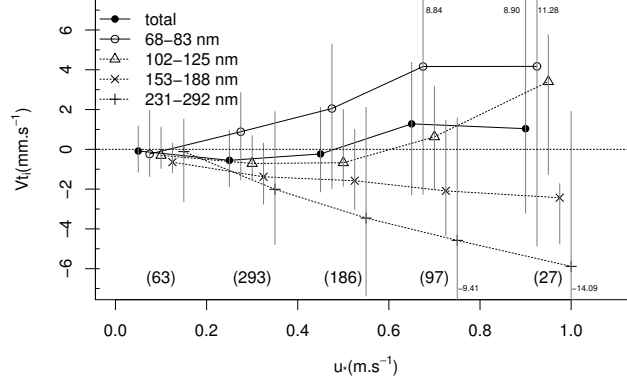


Figure 14: Evolution of transfer velocity (median) with the friction velocity. The symbols represent the median velocity within each friction velocity bin. The number of samples in each bin is given in brackets. The error bars represent the interquartile ranges (25-75%). Symbols abscissas are slightly shifted in order to make the interquartile ranges visible. Quartile values are labelled when they are outside the scale.

3.2.3. Transfer velocity and leaf area index

Leaf area index has been thought to play a central role in particle deposition, as it scales the amount of surface collecting particles. To our knowledge, no experimental evidence on real forests has been presented to test this hypothesis.

595 The present measurement campaign is valuable in this respect as it extended late in the fall and included leaf senescence and partial leaf fall: By the end of the campaign, the leaf area index was reduced by 70 %, ranging from 13 (two-sided) to about 5 (see supplementary material Appendix C).

Grouping the transfer velocities according to LAI (smaller or larger than 11)
600 reveals a consistent pattern in the decrease of the transfer velocity with LAI (Tab. 6). A non-parametric statistical test (Kolmogorov-Smirnov) shows the significance of the difference between the two distributions.

All size bins displayed a more negative transfer velocity when the leaf area index was larger, which highlighted a stronger deposition influence at high leaf
605 area. Based on the KS test, six out of eight reliable size bins displayed a p-

Size bin	Vt_i LAI $\in [5; 11[$	Vt_i LAI $\in [11; 13]$	p-value (Signif. level)	$\frac{\Delta Vt_i}{Vt_i}$ (%)	$\frac{\Delta Vt_{modi}}{Vt_{modi}}$ (%)
total count	0.09 (285)	-0.56 (384)	$4 \cdot 10^{-4}$ (***)	312.4	NA
55-068 nm	2.62 (327)	1.79 (432)	0.018 (*)	39.4	42.2
68-083 nm	1.47 (288)	1.24 (376)	0.031 (*)	16.7	43.2
83-102 nm	1.12 (239)	0.39 (274)	0.111 ()	103.3	41.4
102-125 nm	-0.02 (223)	-0.83 (256)	0.004 (**)	173.1	43.2
125-153 nm	-0.39 (223)	-1.26 (277)	$2 \cdot 10^{-4}$ (***)	100.3	40.1
153-188 nm	-1.04 (232)	-1.75 (305)	$3 \cdot 10^{-4}$ (***)	49	41.3
188-231 nm	-1.65 (227)	-2.51 (294)	0.011 (*)	39.5	34.9
231-292 nm	-2.53 (222)	-2.90 (305)	0.098 (.)	14.1	39.2
292-359 nm	-3.14 (239)	-7.21 (324)	$2 \cdot 10^{-6}$ (***)	86.6	33.6
359-440 nm	-4.74 (265)	-7.68 (330)	0.005 (**)	48	37
440-541 nm	3.89 (300)	-16.65 (378)	$4 \cdot 10^{-9}$ (***)	219.2	37.8
541-664 nm	11.12 (315)	17.91 (380)	$1 \cdot 10^{-5}$ (***)	50.1	40.6
664-815 nm	29.97 (327)	56.04 (191)	$1 \cdot 10^{-5}$ (***)	77.1	52.5
815-1000 nm	37.6 (266)	55.25 (108)	0.278 ()	44.5	60.7

Table 6: Influence of the leaf area index on the transfer velocity. Median are given in mm.s^{-1} . Only the quality 1 to 3 are used and the number of samples in each group is given in brackets. The significance level of the KS test are : '***' for $p \leq 0.001$, '**' for $0.001 < p \leq 0.01$, '*' for $0.01 < p \leq 0.05$, '.' for $0.05 < p \leq 0.1$, ' ' for $0.1 < p$.

value smaller than 0.05. The relative difference of the transfer velocity was also calculated between the medians of the two groups. While the model predicted differences between 35 and 43 %, measurements exhibited highly variable difference among the size bins, between 17 and 173 %. This variability could not be related to difference of aerosol size.

We investigated if the seasonal change in the transfer velocity might be related to changes of other parameters than LAI. To do so, we applied the same statistical test to other parameters grouped by LAI (Tab. 7). When the LAI decreased, the roughness length decreased as well, the horizontal wind increased while the friction velocity, stability parameter and the heat fluxes were not statistically

	LAI $\in [5; 11[$	LAI $\in [11; 13]$	p-value	Signif. level
z_0 (m)	1.26	1.62	$3 \cdot 10^{-6}$	***
u_* (m.s $^{-1}$)	0.41	0.39	0.451	
ξ (-)	0.08	0.06	0.752	
$\overline{u_R}$ (m.s $^{-1}$)	2.54	2.12	$7 \cdot 10^{-9}$	***
Hc (W.m $^{-2}$)	-20.93	-17.75	0.130	
LEc (W.m $^{-2}$)	19.5	27.39	0.025	*

Table 7: Influence of the leaf area index on the median of parameters. The significance level of the KS test are : '***' for $p \leq 0.001$, '**' for $0.001 < p \leq 0.01$, '*' for $0.01 < p \leq 0.05$, '.' for $0.05 < p \leq 0.1$, ' ' for $0.1 < p$.

different between the two groups. The increase of the horizontal wind, related to the roughness length by the log law, implied an increase of the wind velocity inside the canopy as well. Based on the deposition model, when the wind velocity increased, the deposition rate per unit of leaf area by Brownian diffusion and interception, active for Aitken and accumulation modes particles, increased as well. But, because the amount of available collecting leaf surfaces decreased, the overall deposition was lower.

This is to our knowledge the first time that the influence of the Leaf Area Index on the particle transfer velocity has been documented by a measurement campaign on a real forest, moreover using a eddy-correlation technique.

3.2.4. Transfer velocity and stability

Stability has been mentioned in the literature as a possible driver of particle transfer, i.e. that the non-dimensional transfer velocity significantly increases in unstable conditions (Wesely et al., 1985; Lamaud et al., 1994). Empirical relationships were proposed by these authors but so far no theory has been developed to explain these observations.

We investigated the influence of the stability by splitting the data in 3 groups and applying the same KS statistical test on the distributions of the transfer velocity. One group corresponded to unstable conditions ($\xi \leq 0$) and the other two

635 respectively to slightly stable ($\xi \in]0; 0.15]$) and moderately stable ($\xi > 0.15$) conditions (Tab. 8). Distinguishing two groups under stable conditions was dictated by the need to have similar numbers of samples in each group.

An influence of instability on the non-dimensional transfer velocity was consis-

Size bin	$1000Vt_i/u_*$ $\xi \leq 0$ ①	$1000Vt_i/u_*$ $\xi \in]0; 0.15]$ ②	$1000Vt_i/u_*$ $\xi > 0.15$ ③	p (Signif. level) ①vs②	p (Signif. level) ②vs③
total count	1.3 (210)	-0.9 (222)	-1.4 (237)	0.003 (**)	0.821 ()
55-068 nm	8.7 (248)	4 (254)	4.2 (257)	$4 \cdot 10^{-4}$ (***)	0.786 ()
68-083 nm	7.1 (216)	3.4 (223)	0.8 (225)	$4 \cdot 10^{-5}$ (***)	0.362 ()
83-102 nm	5.4 (173)	1.1 (169)	-0.3 (171)	$1 \cdot 10^{-7}$ (***)	0.032 (*)
102-125 nm	1.7 (161)	-2.2 (160)	-2.3 (158)	$2 \cdot 10^{-5}$ (***)	0.602 ()
125-153 nm	-1.8 (166)	-1.4 (167)	-3.4 (167)	0.234 ()	0.005 (**)
153-188 nm	-3.7 (172)	-3.2 (179)	-3.7 (186)	0.372 ()	0.837 ()
188-231 nm	-5.5 (163)	-5.7 (186)	-5.3 (172)	0.581 ()	0.267 ()
231-292 nm	-7.4 (166)	-6.7 (188)	-5.8 (173)	0.039 (*)	0.069 (.)
292-359 nm	-10.9 (185)	-9.3 (198)	-16.6 (180)	0.112 ()	0.014 (*)
359-440 nm	-13.9 (211)	-16.5 (198)	-11.6 (186)	0.894 ()	0.033 (*)
440-541 nm	-21.1 (232)	-19.5 (226)	-24.1 (220)	0.267 ()	0.259 ()
541-664 nm	-29.6 (232)	47.6 (235)	32.3 (228)	0.237 ()	0.173 ()
664-815 nm	82.2 (200)	88.9 (166)	86.7 (152)	0.993 ()	0.749 ()
815-1000 nm	-91.7 (149)	154.2 (125)	146.9 (100)	0.098 (.)	0.365 ()

Table 8: Influence of the stability on the non-dimensional transfer velocity. Medians are displayed. Only the quality 1 to 3 are used and the number of samples in each group is given in brackets. The significance level of the KS test are : '***' for $p \leq 0.001$, '**' for $0.001 < p \leq 0.01$, '*' for $0.01 < p \leq 0.05$, '.' for $0.05 < p \leq 0.1$, ' ' for $0.1 < p$.

640 tently noticeable for particles smaller than 125 nm. There, the non-dimensional transfer velocity was larger under unstable than stable conditions. The difference was statistically significant for all particle bins below 125 nm, as well as the total number ($p \leq 0.01$). Above 125 nm, the differences between unstable and stable regimes were not significant. Between slightly stable and moderately stable conditions, non-dimensional transfer velocity was not significantly

645 different.

Conclusions

This 8-week campaign was to our knowledge the first one to document size-resolved number fluxes of Aitken and accumulation modes' particles on a temperate broadleaf forest. We observed a majority of upward fluxes (emission) for the size bins smaller than 100 nm ($r_+ = 55\%$ on average) and a majority of downward fluxes (deposition) for particles larger than 100 nm ($r_+ = 38\%$ on average). The pattern of emission and deposition showed a consistent diurnal cycle, with the preference for deposition of larger particles peaking around midday, consistent with bulk CPC measurements (Rannik et al., 2009) and a preference for emission of smaller particles peaking in the late afternoon. For the reliably detected size bins (68-292 nm), the median transfer velocity ranged from $+1.34$ to -2.69 mm.s⁻¹ (-0.21 mm.s⁻¹ for the total count) and exhibited a diurnal pattern.

Reasons were brought forward to explain the consistently upward fluxes of the smallest particles, related either to the nucleation of secondary organic aerosol (Farmer et al., 2015) or to the ill-characterized correction for particle deliquescence due to potential fluctuation dampening inside the tubes and instrument, non-ideal determination of the coefficient β and possible inadequate formulation of the correction itself.

The present flux measurements for particles larger than 100 nm were consistent with the scarce data sets existing in the literature. It confirms the role of some of the main drivers of particle deposition, namely particle size, friction velocity and, to our knowledge for the first time on a real site, leaf area index. Instability was found to have an impact on particle transfer, but only for the smallest particles (below 125 nm). The role of particle size in the stability influence on the transfer was not documented in earlier studies (Wesely et al., 1985; Lamaud et al., 1994).

The present data spanned early to late in the fall and allowed us to document

for the first time the impact of the leaf senescence and the abrupt decrease of
675 the Leaf Area Index on particle transfer. Results showed that all particle size
bins showed reduced deposition as leaf area index decreased.

The comparison with other measurements on broadleaf and coniferous forests
did not clearly emphasize the influence of leaf shape and size, though hypothe-
sized by the theory (Fig. 13). Indeed, transfer velocity is smaller in a coniferous
680 dataset (Deventer et al., 2015) than in another broadleaf dataset (Pryor et al.,
2009). This influence was probably obscured by the variability of the measure-
ment conditions and the measurement uncertainties themselves.

The mechanistic model was shown to reproduce particle fluxes smaller than 100
nm but appeared to under-estimate measurements in the 100-500 nm range.
685 Considering the median of the measurement campaigns, this under-estimation
was of a factor ranging from 2 to 7. Notwithstanding the variability of the mea-
surement conditions and uncertainties, it likely means that the model is missing
or inadequately describing some of the processes responsible for deposition of
particles in the accumulation mode (leaf fluttering, interception on leaf micro-
690 roughness, intermittency of the turbulent transfer in the canopy).

In order to gain more insight in the particle transfer and the fast physical and
chemical processes participating to it, particle number flux measurements could
be run side-by-side with particle chemistry fluxes measurements. Such measure-
ments would be particularly informative to better understand upward fluxes,
695 such as those highlighted in the present paper.

Acknowledgements

We are grateful to the Haliburton forest staff and owner for their support, as
well as Ting Zheng and Jing Ming Chen (Dept of Geography, Univ. of Toronto)
for sharing the TRAC instrument LAI data. The UHSAS and SMPS instru-
700 ments were contributed by the Canadian Aerosol Research Network, funded by
the Canada Foundation for Innovation.

Ahlm, L., Nilsson, E.D., Krejci, R., Mårtensson, E.M., Vogt, M., Artaxo, P.,

2009. Aerosol number fluxes over the amazon rain forest during the wet season. *Atmospheric Chemistry and Physics* 9, 9381–9400.
- 705 Baldocchi, D.D., Hicks, B.B., Meyers, T.P., 1988. Measuring biosphere-atmosphere exchanges of biologically related gases with micrometeorological methods. *Ecology* 69, 1331–1340.
- Brockmann, J.E., 2001. Sampling and transport of aerosols, in: Baron, P., Willeke, K. (Eds.), *Aerosol Measurement: Principles, Techniques, and Applications*. Wiley-Interscience, Hoboken, pp. 143–195.
- 710 Brockmann, J.E., 2001. Sampling and transport of aerosols, in: Baron, P., Willeke, K. (Eds.), *Aerosol Measurement: Principles, Techniques, and Applications*. Wiley-Interscience, Hoboken, pp. 143–195.
- Buzorius, G., Rannik, Ü., Mäkelä, J.M., Vesala, T., Kulmala, M., 2000. Vertical aerosol fluxes measured by eddy covariance methods and deposition of nucleation mode particles above a scots pine forest in southern finland. *Journal of Geophysical Research* 105, 19905–19916.
- 715 Cai, Y., Montague, D.C., Mooiweer-Bryan, W., Deshler, T., 2008. Performance characteristics of the ultra high sensitivity aerosol spectrometer for particles between 55 and 800 nm: Laboratory and field studies. *Journal of aerosol science* 39, 759–769.
- Chen, J.M., Cihlar, J., 1995. Plant canopy gap-size analysis theory for improving optical measurements of leaf area index. *Applied Optics* 34, 6211–6222.
- 720 Chen, J.M., Cihlar, J., 1995. Plant canopy gap-size analysis theory for improving optical measurements of leaf area index. *Applied Optics* 34, 6211–6222.
- Davidson, C.I., Miller, J.M., Pleskow, M.A., 1982. The influence of surface structure on predicted particle dry deposition to natural grass canopies. *Water, Air and Soil Pollution* 08, 22–43.
- Deventer, M.J., Held, A., El-Madany, T.S., Klemm, O., 2015. Size-resolved eddy covariance fluxes of nucleation to accumulation mode aerosol particles over a coniferous forest. *Agricultural and Forest Meteorology* 214-215, 328–340.
- 725 Deventer, M.J., Held, A., El-Madany, T.S., Klemm, O., 2015. Size-resolved eddy covariance fluxes of nucleation to accumulation mode aerosol particles over a coniferous forest. *Agricultural and Forest Meteorology* 214-215, 328–340.
- Environment Canada, 2004. 2004 Canadian acid deposition science assessment. Technical Report ISBN 0-662-38754-6. Environment Canada, Meteorological Service of Canada, Downsview, Ontario, Canada.

- 730 Fairall, C.W., 1984. Interpretation of eddy-correlation measurements of particulate deposition and aerosol flux. *Atmospheric Environment - Part A General Topics* 18, 1329–1337.
- Farmer, D.K., Chen, Q., Kimmel, J.R., Docherty, K.S., Nemitz, E., Artaxo, P.A., Cappa, C.D., Martin, S.T., Jimenez, J.L., 2015. Chemically resolved
735 particle fluxes over tropical and temperate forests. *Aerosol Science and Technology* 47, 818–830.
- Farmer, D.K., Kimmel, J.R., Phillips, G., Docherty, K.S., Worsnop, D.R., Sueper, D., Nemitz, E., Jimenez, J.L., 2011. Eddy-covariance measurements with high-resolution time-of-flight aerosol mass spectrometry: A new
740 approach to chemically-resolved aerosol fluxes. *Atmospheric Measurement Techniques* 4, 1275–1289.
- Foken, T., Göckede, M., Mauder, M., Mahrt, L., Amiro, B., Munger, W., 2004. Post-field data quality control, in: Lee, X., Massman, W., Law, B. (Eds.), *Handbook of Micrometeorology*. Kluwer Academic Publishers, Netherlands.
- 745 Fors, E.O., Swietlicki, E., Svenningsson, B., Kristensson, A., Frank, G.P., Sporre, M., 2011. Hygroscopic properties of the ambient aerosol in southern sweden – a two year study. *Atmospheric Chemistry and Physics* 11, 8343–8361.
- Fowler, D., Pilegaard, K., Sutton, M.A., Ambus, P., Raivonen, M., Duyzer, J., Simpson, D., Fagerli, H., Fuzzi, S., Schjoerring, J.K., Granier, C., Neftel, A., Isaksen, I.S.A., Laj, P., Maione, M., Monks, P.S., Burkhardt, J., Daem-
750 mgen, U., Neirynck, J., Personne, E., Wichink-Kruit, R., Butterbach-Bahl, K., Flechard, C., Tuovinen, J.P., Coyle, M., Gerosa, G., Loubet, B., Altimir, N., Gruenhage, L., Ammann, C., Cieslik, S., Paoletti, E., Mikkelsen, T.N.,
755 Ro-Poulsen, H., Cellier, P., Cape, J.N., Horvath, L., Loreto, F., Niinemets, U., Palmer, P.I., Rinne, J., Misztal, P., Nemitz, E., Nilsson, D., Pryor, S., Gallagher, M.W., Vesala, T., Skiba, U., Brüeggemann, N., Zechmeister-Boltenstern, S., Williams, J., O’Dowd, C., Facchini, M.C., de Leeuw, G.,

- Flossman, A., Chaumerliac, N., Erisman, J.W., 2009. Atmospheric composition change: Ecosystems-atmosphere interactions. *Atmospheric Environment* 43, 5193–5267.
- Gallagher, M.W., Beswick, K.M., Duyzer, J., Westrate, H., Choularton, T.W., Hummelshøj, P., 1997. Measurements of aerosol fluxes to speulder forest using a micrometeorological technique. *Atmospheric Environment* 31, 359–373.
- Geddes, J.A., Murphy, J.G., 2014. Observations of reactive nitrogen oxide fluxes by eddy covariance above two midlatitude north american mixed hardwood forests. *Atmospheric Chemistry and Physics* 14, 2939–2957.
- Geddes, J.A., Murphy, J.G., Schurman, J., Petroff, A., Thomas, S.C., 2014. Net ecosystem exchange of an uneven-aged managed forest in central ontario, and the impact of a spring heat wave event. *Agricultural and Forest Meteorology* 198–199, 105–115.
- Gordon, M., Staebler, R.M., Liggio, J., Vlasenko, A., Li, S.M., Hayden, K., 2011. Aerosol flux measurements above a mixed forest at borden, ontario. *Atmospheric Chemistry and Physics* 11, 6773–6786.
- Gradowski, T., Thomas, S.C., 2006. Phosphorus limitation of sugar maple growth in central ontario. *Forest Ecology and Management* 226, 104–109.
- Gradowski, T., Thomas, S.C., 2008. Responses of acer saccharum canopy trees and saplings to p, k and lime additions under high n deposition. *Tree Physiology* 28, 173–185.
- Halldin, S., 1985. Leaf and bark area distribution in a pine forest, in: Hutchinson, B.A., Hicks, B.B. (Eds.), *The Forest–Atmosphere Interaction*. D. Reidel, Dordrecht, p. 39–58.
- Harman, I.N., Finnigan, J.J., 2007. A simple unified theory for flow in the canopy and roughness sublayer. *Boundary-Layer Meteorology* 123, 339–363.

- 785 Held, A., Niessner, R., Bosveld, F., Wrzesinsky, T., Klemm, O., 2007. Evaluation and application of an electrical low pressure impactor in disjunct eddy covariance aerosol flux measurements. *Aerosol Science and Technology* 41, 510–519.
- Held, A., Nowak, A., Wiedensohler, A., Klemm, O., 2006. Field measurements
790 and size-resolved model simulations of turbulent particle transport to a forest canopy. *Aerosol Science* 37, 786–798.
- Horst, T.W., 1973. Spectral transfer functions for a three-component sonic anemometer. *Journal of applied meteorology* 12, 1072–1075.
- Junge, C.E., 1963. *Air Chemistry and radioactivity*, vol.4. Academic Press,
795 New York.
- Kaimal, J.C., Finnigan, J.J., 1994. *Atmospheric boundary layer flows*. Oxford University Press, New York Oxford.
- Kaimal, J.C., Wyngaard, J.C., Izumi, Y., Coté, O., 1972. Spectral characteristics of surface-layer turbulence. *Quarterly journal Royal Meteorological Society* 98, 563–589.
800
- Kolmogorov, A.N., 1941. The local structure of turbulence in incompressible viscous fluid for very large reynolds numbers. *Proceedings of the USSR Academy of Sciences*, in Russian 30, 299–303.
- Kowalski, A.S., 2001. Deliquescence induces eddy covariance and estimable dry
805 deposition errors. *Atmospheric Environment* 35, 4843–4851.
- Lamaud, E., Brunet, Y., Labatut, A., Lopez, A., Fontan, J., Druilhet, A., 1994. The landes experiment: Biosphere-atmosphere exchanges of ozone and aerosol particles above a pine forest. *journal of Geophysical Research* 99, 16511–16521.
- 810 Lee, X., W., M., (eds), L.B.E., 2004. *Handbook of micrometeorology. A guide for surface flux measurement and analysis*. Kluwer Academic Press, Dordrecht.

- Liu, H., Peters, G., Foken, T., 2001. New equations for sonic temperature variance and buoyancy heat flux with an omnidirectional sonic anemometer. *Boundary-Layer Meteorology* 100, 459–468.
- 815 Loescher, H., Ocheltree, T., Tanner, B., Swiatek, E., Dano, B., Wong, J., Zimmerman, G., Campbell, J., Stock, C., Jacobsen, L., Shiga, Y., Kollas, J., Liburdy, J., Law, B., 2005. Comparison of temperature and wind statistics in contrasting environments among different sonic anemometer–thermometers. *Agricultural and Forest Meteorology* 133, 119–139.
- 820 Lumley, J.L., Panofsky, H.A., 1964. The structure of atmospheric turbulence. Interscience publishers, New York.
- Mammarella, I., Rannik, Ü., , Aalto, P., Keronen, P., Vesala, T., Kulmala, M., 2011. Long-term aerosol particle flux observations. part ii: Particle size statistics and deposition velocities. *Atmospheric Environment* 45, 3794–3805.
- 825 Massman, W.J., 1991. The attenuation of concentration fluctuations in turbulent flow through a tube. *Journal of Geophysical Research-Atmospheres* 96, 15269–15273.
- Mauder, M., Liebethal, C., Göckede, M., Leps, J.P., Beyrich, F., Foken, T., 2006. Processing and quality control of flux data during litfass-2003. 830 *Boundary-Layer Meteorology* 121, 67–88.
- Meyer, N.K., Duplissy, J., Gysel, M., Metzger, A., Dommen, J., Weingartner, E., Alfarra, M.R., Prevot, A.S.H., Fletcher, C., Good, N., McFiggans, G., Jonsson, A.M., Hallquist, M., Baltensperger, U., Ristovski, Z.D., 2009. Analysis of the hygroscopic and volatile properties of ammonium sulphate seeded 835 and unseeded soa particles. *Atmospheric Chemistry and Physics* 9, 721–732.
- Moore, C.J., 1986. Frequency response corrections for eddy correlation systems. *Boundary-Layer Meteorology* 37, 17–35.

- Nemitz, E., Gallagher, M.W., Duyzer, J.H., Fowler, D., 2002. Micrometeorological measurements of particle deposition velocities to moorland vegetation. Quarterly Journal of the Royal Meteorological Society 128, 2281–2300.
- 840 Nemitz, E., Jimenez, J.L., Huffman, J.A., Ulbrich, I.M., Canagaratna, M.R., Worsnop, D.R., Guenther, A.B., 2008. An eddy-covariance system for the measurement of surface/atmosphere exchange fluxes of submicron aerosol chemical species—first application above an urban area. Aerosol Science and Technology 42, 636–657.
- 845 Nemitz, E., Sutton, M.A., Wyers, G.P., Otjes, R.P., Mennen, M.G., van Putten, E.M., Gallagher, M.W., 2004. Gas-particle interactions above a dutch heathland: II. concentrations and surface exchange fluxes of atmospheric particles. Atmospheric Chemistry and Physics 4, 1007–1024.
- 850 Nock, C.A., Caspersen, J.P., Thomas, S.C., 2008. Large ontogenetic declines in intra-crown leaf area index in two temperate deciduous tree species. Ecology 89, 744–753.
- Obukhov, A.M., 1971. Turbulence in an atmosphere with a non-uniform temperature. Boundary-Layer Meteorology 2, 7–29.
- 855 Parkhurst, D.F., Duncan, P.R., Gates, D.M., Kreith, F., 1968. Wind tunnel modeling of convection of heat between air and broad leaves of plants. Agricultural Meteorology 5, 33–47.
- Petroff, A., Zhang, L., 2010. Development and validation of a size-resolved particle dry deposition scheme for application in aerosol transport models. Geoscientific Model Development 3, 753–769.
- 860 Petroff, A., Zhang, L., Pryor, S.C., Belot, Y., 2009. An extended dry deposition model for aerosols onto broadleaf canopies. Journal of Aerosol Science 40, 218–240.
- Pryor, S.C., 2006. Size-resolved particle deposition velocities of sub-100 nm diameter particles over a forest. Atmospheric Environment 40, 6192–6200.
- 865

- Pryor, S.C., Barthelmie, R.J., Spaulding, A.M., Larsen, S.E., Petroff, A., 2009. Size-resolved fluxes of sub-100-nm particles over forests. *Journal of Geophysical Research* 114, D18212.
- 870 Pryor, S.C., Larsen, S.E., Sørensen, L.L., Barthelmie, R.J., Grönholm, T., Kulmala, M., Launiainen, S., Rannik, Ü., Vesala, T., 2007. Particle fluxes over forests: Analyses of flux methods and functional dependencies. *Journal of Geophysical Research* 112, D07205.
- Rannik, Ü., Aalto, P., Keronen, P., Vesala, T., Kulmala, M., 2003. Interpretation of aerosol particle fluxes over a pine forest: Dry deposition and random
875 errors. *Journal of Geophysical Research* D17, 4544.
- Rannik, Ü., Mammarella, I., Aalto, P., Keronen, P., Vesala, T., Kulmala, M., 2009. Long-term aerosol particle flux observations part i: Uncertainties and time-average statistics. *Atmospheric Environment* 43, 3431–3439.
- Rannik, Ü., Vesala, T., Keskinen, R., 1997. On the damping of temperature
880 fluctuations in a circular tube relevant to the eddy covariance measurement technique. *Journal of Geophysical Research* 102, 12789–12794.
- Raupach, M., 1994. Simplified expressions for vegetation roughness length and zero-plane displacement as a function of the canopy height and the area index. *Boundary-Layer Meteorology* 71, 211–216.
- 885 Schotanus, P., Nieuwstadt, F.T.M., Bruin, H.A.R., 1983. Temperature measurement with a sonic anemometer and its application to heat and moisture fluxes. *Boundary-Layer Meteorology* 26, 81–93.
- Swietlicki, E., Zhou, J., Covert, D.S., Hämeri, K., Busch, B., Väkeva, M., Dusek, U., Berg, O.H., Wiedensohler, A., Aalto, P., Mäkelä, J., Martinsson, B.G., Pappaspiropoulos, G., Mentes, B., Frank, G., Stratmann, F., 2000. Hygroscopic properties of aerosol particles in the north-eastern atlantic during ace-2. *Tellus B* 52, 201–227.

- Thomas, R.M., 2007. Measurement of Speciated Aerosol Fluxes. Ph.D. thesis. School of Earth and Environmental Sciences, Manchester, UK.
- 895 Thomas, S.C., Winner, W.E., 2000. A rotated ellipsoidal angle density function improves estimation of foliage inclination distributions in forest canopies. *Agricultural and forest meteorology* 100, 19–24.
- Vickers, D., Mahrt, L., 1997. Quality control and flux sampling problems for tower and aircraft data. *journal of Atmospheric and Oceanic Technology* 14, 900 512–526.
- Vong, R.J., Vickers, D., Covert, D.S., 2004. Eddy correlation measurements of aerosol deposition to grass. *Tellus B* 56, 105–117.
- Vong, R.J., Vong, I.J., Vickers, D., Covert, D.S., 2010. Size-dependent aerosol deposition velocities during bearpex'07. *Atmospheric Chemistry and Physics* 905 10, 5749–5758.
- Wang, J.M., Murphy, J.G., Geddes, J.A., Winsborough, C.L., Basiliko, N., , Thomas, S.C., 2013. Methane fluxes measured by eddy covariance and static chamber techniques at a temperate forest in central ontario, canada. *Biogeosciences* 10, 4371–4382.
- 910 Webb, E.K., Pearman, G.I., Leuning, R., 1980. Correction of flux measurements for density effects due to heat and water vapour transfer. *Quarterly journal Royal Meteorological Society* 106, 85–100.
- Wesely, M.L., Cook, D.R., Hart, R.L., Speer, R.E., 1985. Measurements and parametrization of particulate sulfur dry deposition over grass. *journal of* 915 *Geophysical Research* 90, 2131–2143.
- Wilczak, J.M., Oncley, S.P., Stage, S.A., 2001. Sonic anemometer tilt correction algorithms. *Boundary-Layer Meteorology* 99, 127–150.
- Wyngaard, J.C., 1973. On surface layer turbulence, in: Haugen, D. (Ed.), *Proc. Workshop on Micrometeorology*. Science Press, Ephrata.

920 Zhang, L., Gong, S., Padro, J., Barrie, L., 2001. A size-segregated particle dry
deposition scheme for an atmospheric aerosol module. *Atmospheric Environ-*
ment 35, 549–560.

Supplementary materials

Appendix A. Clock synchronisation

925 The wind and particle concentration data were collected by different instru-
ments with different clocks. In order to synchronize them, we needed to ensure,
first, that both series contained all timestamps but also did not contain extra
data generated by the UHSAS PC; and, second, that the drift occurring between
the UHSAS PC clock and a logger clock was taken into account.

930 The first issue resulted from different problems linked to the UHSAS PC clock:
On an irregular basis, the day digit changed before the seconds and milliseconds
finish a 60s cycle. An example of such a timestamps sequence is 8/29/2011
11:59:59.32 PM, 8/29/2011 11:59:59.42 PM and 8/30/2011 11:59:59.53 PM.
These data were removed, together with the data that were not recorded prop-
935 erly by the UHSAS.

Another problem of the UHSAS PC clock, this one more significant, occurred be-
cause sequential UHSAS timestamps were not separated by exactly 0.1 s. Most
of the time, they were varying between 0.08 and 0.12 s, but were infrequently
smaller than 0.05 s or larger than 0.15 s. Though rare, these observations were
940 problematic because they could cause a misalignment of the UHSAS data and
the wind data and forced us to choose if and when they had to be removed from
the data series.

The second issue was that PCs in general had inaccurate clocks and that a drift
occurs between the UHSAS PC and the more precise CR3000 logger clock. This
drift was monitored by recording at 10 Hz the UHSAS PC time and the logger
945 time onto the laptop PC, together with the laptop timestamps. This daily drift
of the UHSAS was about 1.4 s.

The strategy adopted to synchronize the particle data series with the wind series

was the following: First, the UHSAS timestamps were rounded to the closest
950 multiple of 0.1 s. Second, the rounded timestamps were checked for redundancy,
by removing duplicate timestamps. Third, missing records (timestamps with an
interval of 0.2 s or more) were filled with lines of NAs. This method ensures a
proper synchronization of the particle data series with the wind series, though
resulting in a significant loss of the final data (about 4 %). Finally, the lag be-
955 tween the UHSAS clock and the logger clock was subtracted from the UHSAS
signal and the two signals are merged. One could avoid such data preparation
by directly logging the UHSAS data onto the data logger. As part of the flux
calculation, a routine was run to maximize the correlation between the two
signals and find the precise lag (Sec. 1.4).

960 **Appendix B. Quality control**

The first test involved the stationarity of the signals. Following Foken et al.
(2004), signals were split into smaller intervals of 5 min. Statistical parameters
were calculated for each interval and their average was compared with the sta-
tistical parameter calculated over the averaging period of 30 min. Stationarity
flags were given depending on the deviation observed for particle flux, shear
stress and the standard deviation of the particle concentration (Tab. B.9). The
second test involves the flux-variance similarity of Obukhov (1971) that is oc-
curring in a fully developed turbulence. We used the parametrization reported
by Kaimal and Finnigan (1994) linking the standard deviation of the vertical
wind σ_w with the stability parameter:

$$\frac{\sigma_w}{u_*} = \begin{cases} 1.25 (1 - 3\xi)^{1/3} & \text{if } -2 \leq \xi \leq 0 \\ 1.25 (1 + 0.2\xi) & \text{if } 0 \leq \xi \leq 1 \end{cases} \quad (\text{B.1})$$

where ξ is the stability parameter. The quality of turbulence development for
each 30-min period is estimated depending on the departure of the measured
ratio σ_w/u_* from its theoretical value given by Eq. B.1. The overall quality flag
is defined in Table B.10.

Stationarity Flag	$\overline{w'c'_i}$	$\overline{u'w'}$	σ_{ci}
q_{stat}	(deviation in %)	(deviation in %)	(deviation in %)
1	[0; 15]	[0; 30]	[0; 30]
2]15; 30]	[0; 30]	[0; 30]
3	[0; 30]]30; 75]]30; 75]
4]30; 75]	[0; 30]	[0; 30]
5	[0; 75]	[0; 75]	[0; 75]
6	[0; 100]	[0; 100]	[0; 100]
7	[0; 250]	[0; 250]	[0; 250]
8	[0; 1000]	[0; 1000]	[0; 1000]
9	either]1000; ∞]	or]1000; ∞]	or]1000; ∞]

Table B.9: Evaluating the stationarity of the sample based on the turbulent flux, shear stress and the standard deviation of the particle concentration.

Appendix C. Leaf area measurements and linear interpolation

Leaf area index (LAI) measurements were made using litter traps positioned on a grid within 150 m of the flux tower, and seasonal changes in LAI were monitored at an approximate 2-week sampling interval using the TRAC instrument method (Chen and Cihlar, 1995). Peak 2011 LAI (two-sided) was 13, and TRAC measurements indicated a decline in LAI of 70% by the end of the measurement campaign. Measures were linearly interpolated to have a continuous value of the leaf area index (Fig. C.15).

Overall Flag	Stationarity Flag q_{stat}	Developed turbulence (deviation in %)	Orientation of the wind with the sonic (in $^{\circ}$)
1	1	[0; 30]	$\pm 0 - 150$
2	2	[0; 30]	$\pm 0 - 150$
3	1-2]30; 75]	$\pm 0 - 150$
4	3-4	[0; 30]	$\pm 0 - 150$
5	1-4]30; 100]	$\pm 0 - 150$
6	5	[0; 100]	$\pm 0 - 150$
7	1-6	[0; 250]	$\pm 0 - 170$
8	1-8	[0; 1000]	$\pm 0 - 170$
9	either 9	or]1000; ∞]	or $> \pm 170$

Table B.10: Quality control flag system based on Foken et al. (2004).

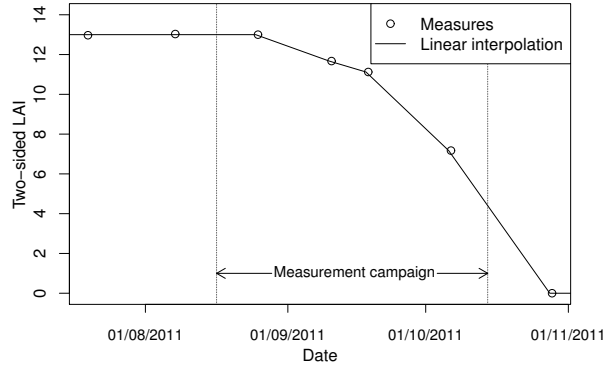


Figure C.15: Evolution of the two sided LAI throughout the campaign. The circles correspond to TRAC measures and the line corresponds to the linear interpolation.